Cell Stem Cell
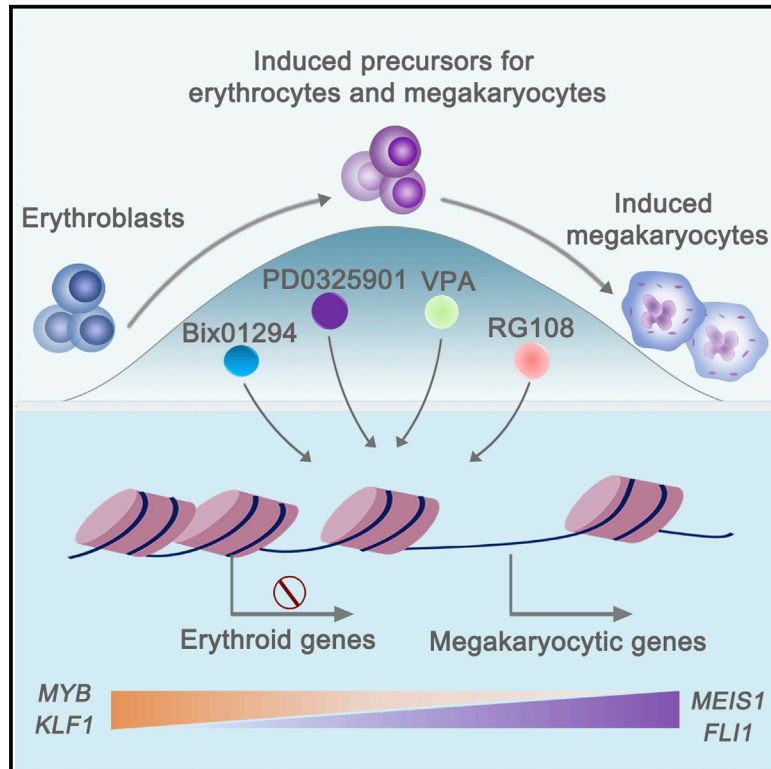
Direct chemical reprogramming of human cord blood erythroblasts to induced megakaryocytes that produce platelets

Graphical abstract

Highlights

- A small-molecule cocktail (4M) converts human cord blood erythroblasts into iMKs

- The iMKs resemble natural MKs and give rise to functional platelets

- ScRNA-seq reveals conversion of EBs into two types of iMKs via an iPEM intermediate

- 4M induces changes in chromatin accessibility dynamics and opens MK-related loci

Authors

Jinhua Qin, Jian Zhang,
Jianan Jiang, ..., Wen Yue, Yanhua Li,
Xuetao Pei

Correspondence

shirlylyh@126.com (Y.L.),
peixt@nic.bmi.ac.cn (X.P.)

In brief

A small-molecule cocktail reprograms human cord blood erythroblasts into induced megakaryocytes with *ex vivo* functionality. The four small molecules extensively remodel the chromatin and induce the dynamic network transition from erythroid master genes to FLI1 and other megakaryopoiesis-related genes via a bi-potent precursor state.

CellPress

Article

Direct chemical reprogramming of human cord blood erythroblasts to induced megakaryocytes that produce platelets

Jinhua Qin,[1,2,5] Jian Zhang,[3,5] Jianan Jiang,[1,5] Bowen Zhang,[1,2] Jisheng Li,[1] Xiaosong Lin,[1] Sihan Wang,[1,2] Meiqi Zhu,[1] Zeng Fan,[1,2] Yang Lv,[1,2] Lijuan He,[2,4] Lin Chen,[1,2] Wen Yue,[1,2] Yanhua Li,[1,2,6,*] and Xuetao Pei[1,2,*]

[1]Stem Cell and Regenerative Medicine Lab, Beijing Institute of Radiation Medicine, Beijing 100850, China
[2]South China Research Center for Stem Cell & Regenerative Medicine, SCIB, Guangzhou 510005, China
[3]Academy of Medical Engineering and Translational Medicine, Tianjin University, Tianjin 300072, China
[4]Institute of Health Service and Transfusion Medicine, Beijing 100850, China
[5]These authors contributed equally
[6]Lead contact
*Correspondence: shirlylyh@126.com (Y.L.), peixt@nic.bmi.ac.cn (X.P.)
https://doi.org/10.1016/j.stem.2022.07.004

SUMMARY

Reprogramming somatic cells into megakaryocytes (MKs) would provide a promising source of platelets. However, using a pharmacological approach to generate human MKs from somatic cells remains an unmet challenge. Here, we report that a combination of four small molecules (4M) successfully converted human cord blood erythroblasts (EBs) into induced MKs (iMKs). The iMKs could produce proplatelets and release functional platelets, functionally resembling natural MKs. Reprogramming trajectory analysis revealed an efficient cell fate conversion of EBs into iMKs by 4M via the intermediate state of bipotent precursors. 4M induced chromatin remodeling and drove the transition of transcription factor (TF) regulatory network from key erythroid TFs to essential TFs for megakaryopoiesis, including *FLI1* and *MEIS1*. These results demonstrate that the chemical reprogramming of cord blood EBs into iMKs provides a simple and efficient approach to generate MKs and platelets for clinical applications.

INTRODUCTION

Platelet (PLT) transfusion is an indispensable life-saving therapy for patients with severe thrombocytopenia (Stubbs et al., 2021). However, due to short shelf life and limited supply donated by human volunteers (Reems et al., 2010; Stroncek and Rebulla, 2007), the supply of PLTs falls behind the increasing demand in response to public health incidents, such as outbreaks of viral hemorrhagic fevers (Kumar et al., 2000). PLTs are generated from megakaryocytes (MKs) in the bone marrow (BM) or lungs (Lefrançais et al., 2017). *Ex-vivo*-engineered generation of MKs and PLTs for clinical transfusion is an appealing approach to providing an alternative source of PLTs (Matsunaga et al., 2006; Moreau et al., 2016; Takayama et al., 2008). Stem cells, including pluripotent stem cells and hematopoietic stem and progenitor cells (HSPCs) derived from cord blood (CB) and mobilized peripheral blood (PB), are considered the most promising cell sources for generating MKs and PLTs (Ito et al., 2018; Nakamura et al., 2014; Xi et al., 2013; Zhang et al., 2021). However, the yields of MKs and PLTs derived from stem cells are not yet sufficient.

Direct cell lineage reprogramming techniques have recently opened a new avenue for obtaining desired cell types for therapeutic purposes (Mahato et al., 2020; Xu et al., 2015; Zhou et al., 2019). Several groups showed that overexpression of different sets of transcription factors (TFs) could directly convert murine or human somatic cells into HSPCs (Cobaleda et al., 2007; Zhang et al., 2018), erythroid progenitors (Capellera-Garcia et al., 2016), and MKs (Pulecio et al., 2016). Despite the initial success of TF overexpression strategies, it poses the risk of exogenous gene incorporation and expression in somatic cells. Pharmacological reprogramming of somatic cells towards hematopoietic cells or MKs is safer than forced gene expression strategies (Xie et al., 2017).

The choice of the initial cell is crucial for developing a method for pharmacological direct cell lineage reprogramming for manufacturing human MKs (Ebrahimi, 2015; Eminli et al., 2009; Polo et al., 2010). Accumulating evidence suggests that changing cell fates within closely related cell types requires less epigenetic remodeling, leading to high conversion efficiency (Hochedlinger and Plath, 2009; Morris and Daley, 2013). Erythroblasts (EBs) are nucleated red blood cells in the CB, BM, and PB. Because EBs and MKs are developmentally related cells that share a common progenitor cell (Xavier-Ferrucio and Krause, 2018) and express similar TFs, such as GATA1 and NFE2 (Klimchenko et al., 2009), EBs are ideal seed cell candidates for
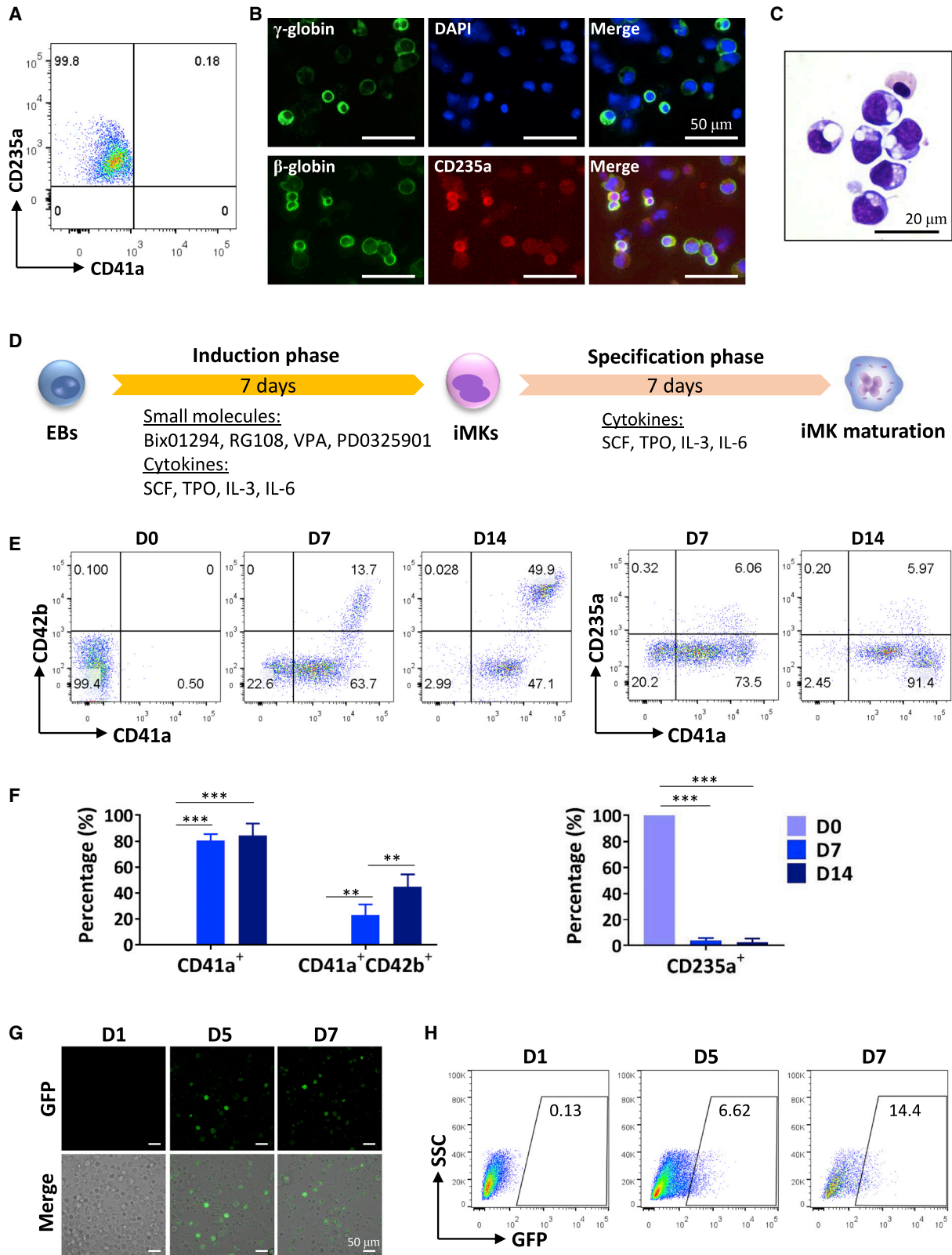
efficient reprogramming towards MKs. Siripin et al. generated MKs and PLTs from BM EBs by ectopic expression of *ERG* and *FLI1* (Siripin et al., 2015). However, a TF-independent MK reprogramming strategy from EBs has not been explored.

CB collection is safe, painless, and easily preserved in public banks. Here, using CB EBs as seed cells, we first screened for small molecules that promoted expression of the MK cell surface markers CD41a and CD42b. We found that a specific combination of the four small molecules (4M), Bix01294, RG108, VPA, and PD0325901, induced the generation of functional MKs directly from CB EBs. The reprogramming path and process were further dissected using single-cell RNA sequencing (scRNA-seq) and assay for transposase-accessible chromatin sequencing (ATAC-seq), which not only revealed an efficient, rapid, and successful MK fate conversion, but also showed that the conversion might involve an intermediate bipotent precursor.

RESULTS

4M cocktail enables activation of the MK fate from EBs

Before starting the cell fate conversion program, CB EBs were expanded and purified as $CD34^-CD123^-CD41a^-CD42b^-CD110^-CD235a^+$ cells using flow cytometry to eliminate HSPCs and MKs (Figure S1A). These purified EBs showed high levels of CD235a, γ-globin, and β-globin expression and no CD41a expression (Figures 1A and 1B), confirming their EB identity without MK contamination. Wright-Giemsa staining showed that the cells had characteristics typical of basophilic EBs (Figure 1C). Initially, the candidate small molecules for lineage reprogramming were narrowed down to three primary categories of reprogramming factors comprised of nine small molecules (9M): (1) epigenetic modulators such as valproic acid (VPA, histone deacetylase inhibitor) (Huangfu et al., 2008; Zhu et al., 2010), Bix01294 (G9a histone methyltransferase inhibitor), and RG108 (DNA methyltransferase inhibitor) (Shi et al., 2008; Wang et al., 2016); (2) signaling pathway inhibitors PD0325901 (MAPK/ERK pathway inhibitor) (Lin et al., 2009), CHIR99021 (GSK3 inhibitor), Forskolin (adenylyl cyclase activator) (Hou et al., 2013; Zhang et al., 2016), Y27632 (ROCK inhibitor) (Cao et al., 2016; Hu et al., 2015), and 2-PCPA (monoamine oxidase inhibitor) (Fu et al., 2015); and (3) metabolic regulator PS48 (Cao et al., 2016; Zhu et al., 2010) (Figure S1B). Because epigenetic modulators are considered to overcome the epigenetic barrier between different types of cells (Ang et al., 2011; Xie et al., 2017), a combination of three epigenetic modulators (Bix01294, RG108, and VPA) was used as a baseline cocktail for screening.

The EB-to-MK conversion was evaluated by flow cytometric analysis of the expression of two MK-specific cell surface markers, CD41a and CD42b. Notably, PD0325901, in combination with three epigenetic modulators, efficiently induced CD41a and CD42b expression on day 7 (Figures S1C and S1D). The combination of four small molecules (4M; Bix01294, RG108, VPA, and PD0325901) was sufficient for efficiently inducing megakaryocytic reprogramming from EBs within 7 days (Figure 1D). No obvious karyotypic alteration was observed in induced cells after 4M induction (Figure S1E). On day 7, the percentages of $CD41a^+$ and $CD41a^+CD42b^+$ cells were 80.30% ± 2.30% and 22.96% ± 3.62%, respectively (Figures 1E and 1F). However, the percentage of $CD41a^+CD42b^+$ cells decreased under 4M reprogramming conditions after culture for another 7 days (Figure S1F). Thus, we defined the MK induction phase under 4M cocktail conditions for 7 days. To ensure successful and efficient generation of induced MKs (iMKs), we designed a two-phase iMK manufacturing protocol involving a reprogramming induction phase (days 0–7) and an MK specification phase (days 8–14) (Figure 1D). After switching to the MK specification phase by withdrawing the 4M cocktail, the percentage of $CD41a^+CD42b^+$ cells significantly increased, reaching 44.60% ± 4.34% on day 14 (Figures 1E and 1F). Notably, the two-phase induction protocol remarkably decreased the expression of the erythroid-specific marker CD235a from the initial 99% purity to 3.96% ± 0.82% on day 7 and to 2.60% ± 1.26% on day 14. A yield of $3.58–6.28×10^8$ $CD41a^+$ iMKs was achieved after two-phase induction initiated from $6×10^7$ EBs derived from 10 mL cord blood (Figure S1G).

The MK-specific PF4 promoter-driven GFP reporter (PF4-GFP) in a lentiviral vector was employed to evaluate whether the 4M reprogramming indeed initiated the conversion of EBs to MK cell fate. By observing GFP^+ cells in EBs infected with lentiviral PF4-GFP, we found that the 4M cocktail gradually initiated GFP expression driven by the PF4 promoter on days 5 and 7 during the reprogramming phase (Figures 1G and 1H) but did not increase transcription activity of the control CMV promoter-GFP (Figure S1H). No prominent GFP expression was observed in EBs transduced with PF4-GFP lentiviruses cultured without 4M (Figure S1I). In summary, these results indicate that the 4M cocktail and subsequent specification-phase induction efficiently converted human CB EBs to phenotypic MKs.

EB-derived iMKs after two-phase induction possess MK characteristics

We then evaluated the characteristics of iMKs derived from the EBs after two-phase induction. Wright-Giemsa staining of the iMKs on day 14 showed that the induced cells had large and polylobulated nuclei with granular accumulation in the cytoplasm (Figure 2A), which is characteristic of MKs. The cell diameters of iMKs were larger than those of the initial EBs (Figure 2B).

Figure 1. Induction of EBs to iMKs with small molecules
(A) Representative flow cytometry dot plots for CD235a and CD41a expression in purified EBs.
(B) Representative confocal pictures of EBs immunostained for β-globin, γ-globin, CD235a, and CD41a. Scale bar, 50 μm.
(C) Wright-Giemsa staining of EBs. Scale bar, 20 μm.
(D) Schematic figure indicates the derivation of iMKs.
(E) Representative flow cytometry dot plots for CD41a, CD42b, and CD235a expression of iMKs on days 7 and 14.
(F) Percentages of $CD41a^+$, $CD41a^+CD42b^+$, and $CD235a^+$ cells on days 7 and 14. Results are expressed as mean ± SEM; n = 5. **p < 0.01; ***p < 0.001.
(G) Representative figures of $PF4\text{-}GFP^+$ cells generated from EBs treated with chemical cocktails on days 1, 5, and 7. Scale bar, 50 μm.
(H) Flow cytometry analysis of $PF4\text{-}GFP^+$ cells generated from EBs treated with chemical cocktails on days 1, 5, and 7.
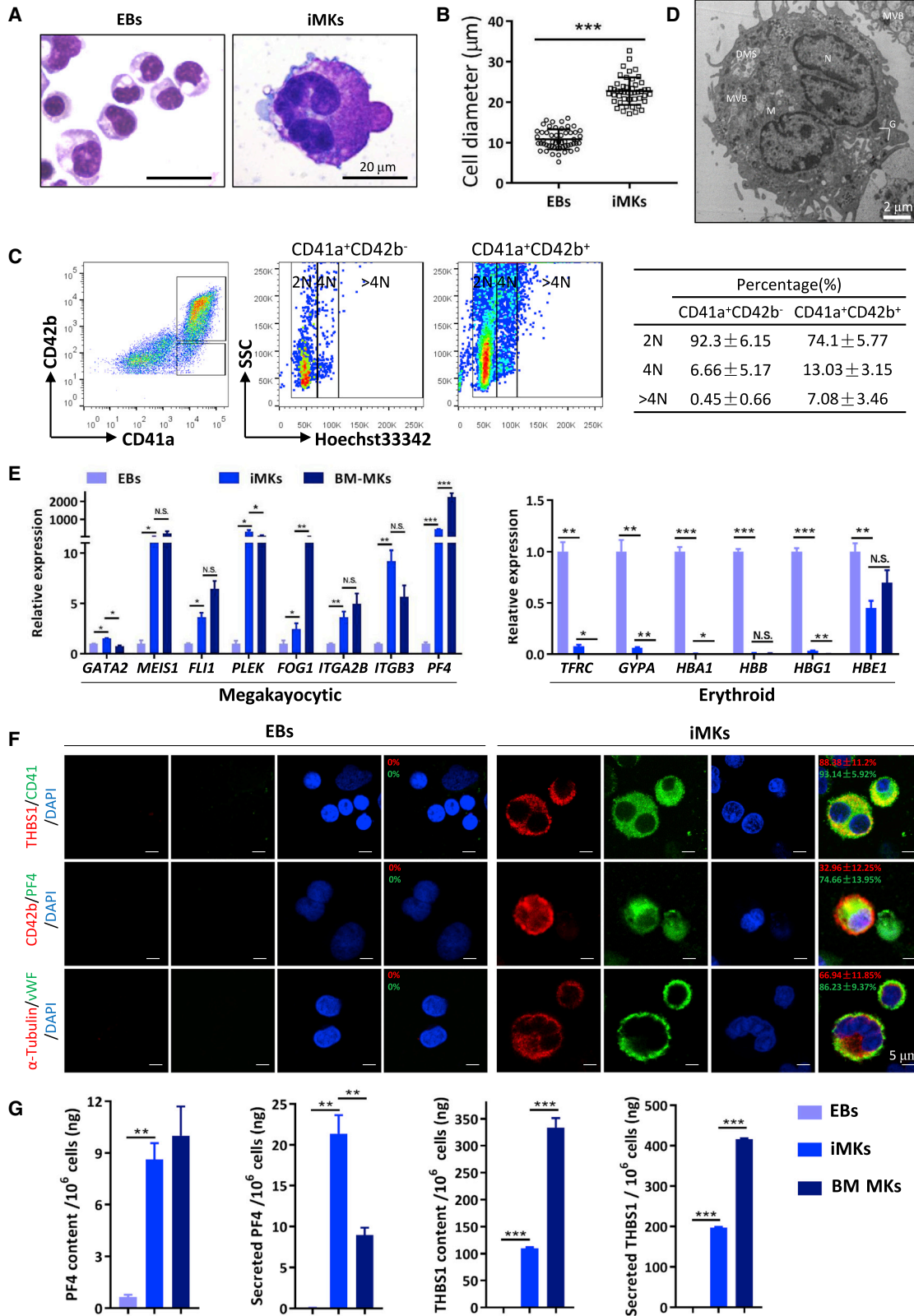
(legend on next page)

We analyzed the nuclear content of iMKs on day 14 using flow cytometry and observed the presence of CD41a$^+$CD42b$^+$ cells with ploidies reaching >4N (Figure 2C). Approximately 13.03% ± 3.15% of CD41a$^+$CD42b$^+$ cells were 4N, and 7.08% ± 3.46% were >4N (Figure 2C). The CD41a$^+$CD42b$^-$ cells also contained a polyploid population, of which about 6.66% ± 5.17% was 4N (Figure 2C). Electron micrographs of iMKs harvested on day 14 showed typical MK organelles, including lobulated nuclei, a developing demarcation membrane system, cytoplasmic multivesicular bodies, and mature granules (Figure 2D).

Similarly, we showed the mRNA expression levels of key MK TFs and markers, such as *GATA2*, *MEIS1*, *FLI1*, *PLEK*, *FOG1*, *ITGA2B*, *ITGB3*, and *PF4*, were significantly upregulated in iMKs on day 14 compared to the initial EBs (Figure 2E). The expression of key erythroid genes, such as *TFRC*, *GYPA*, *HBA1*, *HBB*, and *HBG1*, was significantly decreased and even undetectable in iMKs after 14-day induction (Figure 2E). We then performed immunofluorescence staining to detect characteristic MK protein expression in these cells. We found that ~70% of iMKs on day 14 after two-phase induction expressed high levels of CD41, thrombospondin 1 (THBS1), PF4, vWF, and α-tubulin (Figure 2F). In contrast, EBs did not express these MK-related proteins.

MKs and PLTs can secrete various cytokines, such as PF4 and THBS1, with different functions (Psaila et al., 2012). We evaluated the intracellular synthesis and secretion of several key cytokines by these MK-like cells. PF4 and THBS1 secretion were absent from the initial EBs. Notably, iMKs converted from EBs showed high levels of intracellular and secreted PF4 and THBS1 proteins (Figure 2G). Taken together, these results indicate that the iMKs derived from EBs after two-phase induction resemble bona fide MKs.

iMKs induced from EBs can produce proplatelets and functional platelets

Next, we asked whether iMKs could produce proplatelets and PLTs *in vitro*. The iMKs on day 14 were transferred into MK maturation medium for another 7 days. We found that some iMKs began to develop a proplatelet-like morphology, exhibiting multiple protrusions with long branching extensions that appeared as a string of beads linked by thin cytoplasmic bridges (Figures 3A and 3B). These differentiated proplatelet-like cells expressed CD41, CD42b, and vWF (Figure 3B), indicating that the iMKs matured into proplatelets. Phalloidin staining revealed actin filament networks in the differentiated proplatelets, which play a vital role in the number and branching of proplatelet protrusions (Figure 3B). The iMK-derived proplatelets

were live cells as determined by the results of calcein-AM staining (Figure S2A).

To further evaluate whether these proplatelets can produce PLTs (Robert et al., 2012), the cell culture supernatants were collected and labeled with surface markers for PLT detection. Using flow cytometric analysis, we detected the presence of vital (Propidium Iodide$^-$Annexin V$^-$) PLTs expressing CD41a and CD42b (Figure S2B). The yield of iMK-PLTs was 3.57–12.2×10^9 initiated from 6×10^7 EBs (Figure S1G).Under an electron microscope, these iMK-derived PLTs (iMK-PLTs) showed typical PLT features, including an open canalicular system, granules, and mitochondria, resembling the ultrastructure of natural human PLTs isolated from fresh PB (PB-PLTs) (Figure 3C). Immunofluorescence staining showed that the iMK-PLTs expressed high levels of PLT-characteristic proteins, including CD41, CD42b, THBS1, PF4, vWF, and α-tubulin (Figure 3D), like PB-PLTs. To explore the functionality of iMK-PLTs, we examined the expression of the PLT activation marker CD62P after stimulation with the PLT agonists. CD62P expression intensity presented remarkable increases in iMK-PLTs and PB-PLTs upon stimulation with thrombin or ADP/TRAP (Figures 3E and S2C). Similar to natural PB-PLTs, iMK-PLTs adhered to and spread on fibrinogen-coated surfaces in response to thrombin stimulation, as shown by CD41 and α-tubulin antibody staining (Figure 3F). Importantly, iMK-PLTs demonstrated the ability to form PLT plugs and promote fibrin clot formation and retraction (Figure 3G), indicating that thrombin induced an active state *in vitro*. These data suggest that iMKs induced from EBs by the two-phase induction program can further differentiate into proplatelets and generate functional PLTs *in vitro*.

In vivo production of functional platelets from iMKs

To evaluate whether iMKs could produce functional PLTs *in vivo*, calcein-labeled iMKs or initial EBs were transfused into B-NDG mice (NOD-Prkdc^{scid} IL2rg^{tm1}/Bcgen) with carboplatin-induced thrombocytopenia, which was used to evaluate the *in vivo* function of human MKs and PLTs (Guan et al., 2017; Ulich et al., 1995). The mice were pretreated with clodronate liposomes for macrophage depletion to improve the recovery of human PLTs in mouse circulation (Hu and Yang, 2012; Wang et al., 2015) (Figures 4A and S3). Mouse PB was collected, and flow cytometric detection of calcein-labeled human PLTs was performed on days 1 and 3 after cell transfusion. Notably, iMKs derived from EBs after 14-day induction released human PLTs into the mouse blood circulation. Calcein$^+$ PLT-like cells comprised 4.57% ± 1.35% of the anucleate cells in the circulation of B-NDG mice on day 1 (Figure 4B). In contrast, the EB- or phosphate-buffered saline (PBS)-injected groups contained very few

Figure 2. Characterization of iMKs
(A) Morphology of EBs and iMKs was analyzed using modified Wright-Giemsa staining. Scale bar, 20 μm.
(B) Cell diameter of EBs and iMKs.
(C) Flow cytometry analysis of ploidy among iMKs.
(D) Cell ultrastructure of iMKs was visualized by transmission electron microscopy. N, nucleus; DMS, demarcation membrane system; G, granules; MVB, multivesicular body; M, mitochondria. Scale bar, 2 μm.
(E) qRT-PCR of MK-specific and erythroid-specific genes in EBs, iMKs, and bone-marrow-derived MKs (BM-MKs). Expression levels were normalized to 1 in EBs. Results are expressed as mean ± SEM; n = 3. *p < 0.05; **p < 0.01; ***p < 0.001; N.S., not significant.
(F) Representative confocal pictures of EBs and iMKs immunostained for THBS1, CD41, PF4, CD42b, α-tubulin, and vWF. Scale bar, 5 μm.
(G) Protein level of PF4 and THBS1 in the culture supernatant and cell lysate of EBs, iMKs, and BM-MKs. Results are expressed as mean ± SEM; n = 3. *p < 0.05; **p < 0.01; ***p < 0.001.
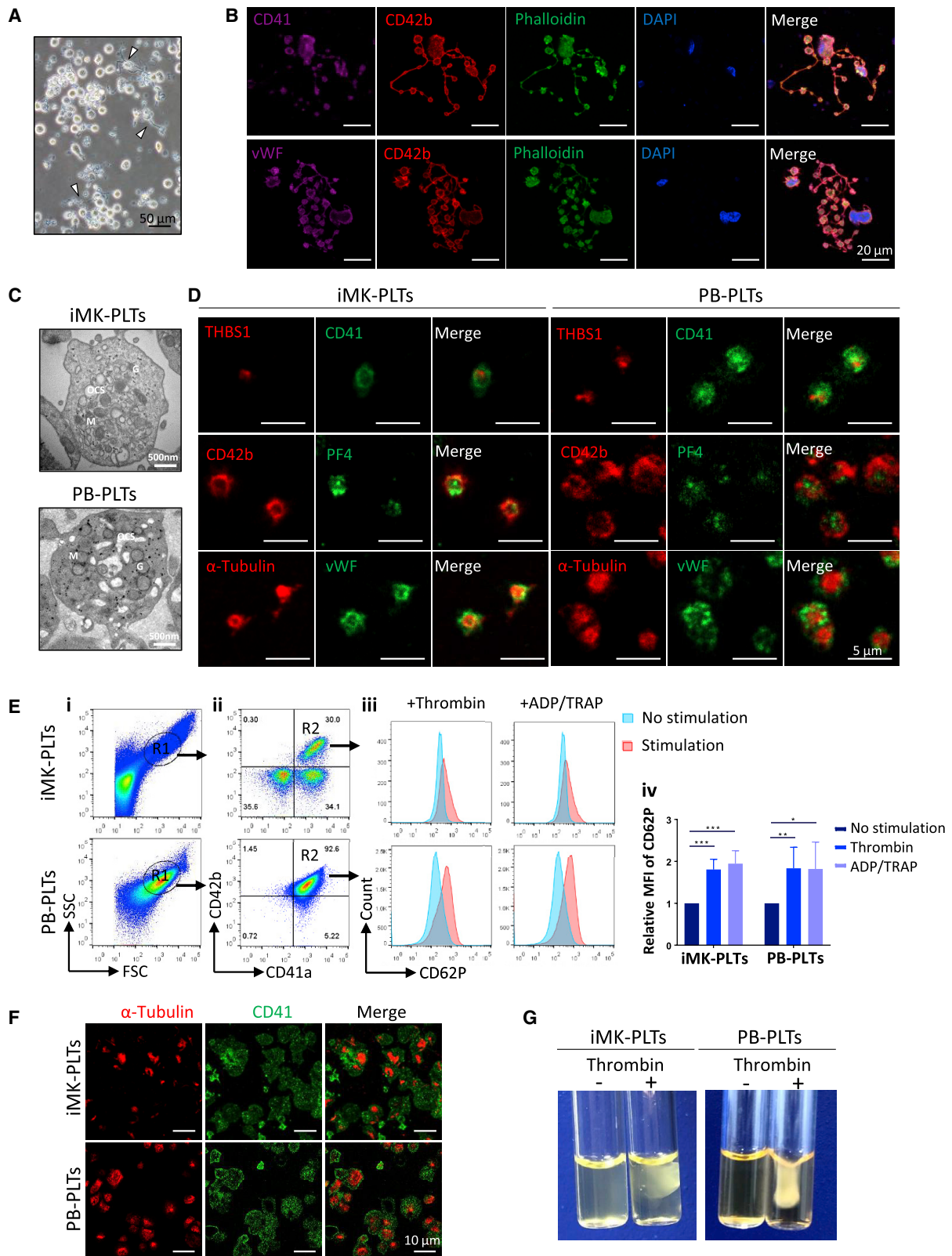
calcein^{+} PLT-like cells (Figure 4B). Similarly, the percentage of human CD41a^{+} PLTs was 0.86% ± 0.22% in iMK-transfused B-NDG mice on day 1 (Figure 4B). The iMKs consistently produced human PLTs *in vivo* until 3 days after transfusion. The calcein[+] human PLT-like cells decreased to 0.80% ± 0.22% on day 3 in the iMK-transfused group (Figure 4C).

To further assess the function of human PLTs produced by calcein-labeled iMKs, we harvested PLT-rich plasma (PRP) from B-NDG mice with carboplatin-induced thrombocytopenia on day 3 after cell transfusion. PRP was preincubated with a phycoerythrin-conjugated anti-human CD41a antibody and evaluated for thrombus formation under flow conditions using a BioFlux 1000z system, an automated microfluidic chamber system. The PRP was perfused into microfluidic chambers coated with collagen, a major subendothelial matrix component. Thrombi were formed in the PRP samples from all three groups (Figure 4D). Under a fluorescence microscope, we observed a significant amount of calcein[+] human PLTs incorporated into the thrombi on the collagen surface in PRP samples from the iMK-infused group, which also showed human CD41a antigen expression (Figure 4D). No obvious human CD41a^{+} and calcein^{+} PLTs were detected in the thrombi formed from the PRP of PBS-injected or EB-transfused groups. Moreover, the contribution of iMK-derived PLTs to thrombi was obviously blocked in the presence of eptifibatide, which selectively blocks human rather than mouse PLTs (Magallon et al., 2011) (Figures S3C and S3D). Our data indicated that iMKs generated from EBs can mature and give rise to functional PLTs *in vivo*.

The scRNA-seq analyses identify the progression of MK fate acquisition and depict the reprogramming path

To finely dissect the reprogramming process of iMKs from EBs, we performed a single-cell gene expression profile analysis of the initial EBs (D0) and reprogrammed cells on days 3 (D3), 5 (D5), and 7 (D7) using the 10x Genomics platform. We captured a total of 24,967 individual cells and identified six transcriptionally distinct clusters labeled as C1–C6 based on t-distributed stochastic neighbor embedding (t-SNE) analysis and Leiden clustering (Traag et al., 2019) (Figures 5A, 5B, and S4A; Table S2). C6 showed a lymphocyte genotype and was removed from downstream analysis. C1 was mainly composed of initial EBs from day 0 (Figure 5C). C2 was more closely related to C1 and showed similarly and gradually decreased expression of some erythroid genes, such as *HBA1*, *GYPA*, *KLF1*, *EPB42*, and *AHSP*; these cells were defined as EB-like cells (Figures 5B, 5D, 5E, and S4B). Transcriptome analysis revealed that most cells in C1 and C2 were in G2M or S phase, indicating that they were in an active proliferative state (Figures S4C and S4D). C3 is an intermediate state among C1, C2, C4, and C5 characterized by high expression of several genes, including *HPGDS*, *LMO4*, and *KIT* (Figures 5D, 5F and S4E). Moreover, C3 expressed both the erythroid-specific TF *MYB* and MK-specific TF *FLI1* (Figures S4B and S4F), indicating that this population might be mainly composed of bipotent precursors for erythrocytes and MKs (PEMs), which were defined as induced PEMs (iPEMs).

C4 and C5 were mainly composed of individual cells from day 7, which showed similar expression levels of key megakaryocytic genes such as *RGS18*, *F2R*, *PPBP*, and *PF4*, hereafter defined as iMK-1 and iMK-2 (Figures 5C and 5D). Compared with the other cell clusters, C4 and C5 showed the most robust expression of various canonical MK-featured genes, including *GP1BA*, *GP9*, *SELP*, *CD9*, *TUBB1*, and *THBS1* (Figures 5G, 5H, and S4F). Moreover, iMK-1 and iMK-2 were more closely related to CB-MKs than PB-MKs based on the gene expression correlation analysis results (Figure S5A). Further comparison of iMK-1 and iMK-2 showed that there were 551 differentially expressed genes (Figure 5I; Table S3). Genes upregulated in iMK-1 were predominantly involved in MK development and PLT functions, such as "PLT aggregation" and "PLT formation" (Figure 5J). In contrast, genes upregulated in iMK-2-enriched biological processes were associated with immune and inflammatory responses (Figure 5J). These data indicated that iMK-1 might be thrombopoiesis-biased MKs and iMK-2 might be immune MKs. CD53 was recently used as a surface marker for immune MKs (Sun et al., 2021); thus, we chose CD53 to distinguish these two populations (Figure S5B) and defined CD41a^{+}CD42b^{+}CD53^{−} cells as iMK-1 and CD41a^{+}CD42b^{+}CD53^{+} cells as iMK-2. We found that both iMK-1 and iMK-2 were present on days 7 and 14, with iMK-1 constituting the majority of CD41a^{+}CD42b^{+} cells (Figures S5C and S5D). These results indicated that our reprogramming system is beneficial for generating thrombopoiesis-biased MKs.

Next, we analyzed the reprogramming trajectory of 4M reprogramming from EBs to iMKs in a pseudotime manner. The cells were ordered and colored according to the predicted pseudotime, which matched the original cell category very well (Figures 6A–6C). Cell-cycle analysis showed that the number of induced cells in G1 significantly increased and their G2M/S cell-cycle score decreased in the late stage of chemical reprogramming (Figure S6A). We identified 1,808 genes that changed significantly as the cells progressed along the trajectory (Table S4). Genes were further grouped and clustered into six

---

Figure 3. Characterization of iMK-PLTs *in vitro*

(A) Phase contrast picture of spontaneous proplatelet-forming iMKs (arrowheads) in suspension culture (day 21). Scale bar, 50 μm.
(B) Proplatelet-forming iMKs on fibrinogen-coated slide immunostained for CD41, CD42b, and vWF were stained with phalloidin. Scale bar, 20 μm.
(C) Transmission electron micrographs of iMK-PLTs and fresh PB-PLTs. OCS, open canalicular system; G, granules; M, mitochondria. Scale bar, 500 nm.
(D) Representative confocal images of iMK-PLTs and PB-PLTs immunostained for THBS1, CD41, PF4, CD42b, α-tubulin, and vWF. Scale bar, 5 μm.
(E) Flow cytometry analysis of CD62P binding to iMK-PLTs and PB-PLTs. (i) Forward scatter (FSC) and side scatter (SSC) analyses of iMK-PLTs. (ii) PLTs from the R1 region analyzed in a 2D plot showing the expression of CD41a and CD42b. (iii) PLTs from the R2 region analyzed in histograms showing CD62P expression on PLTs in response to agonists. (iv) Summarized results showing CD62P binding to iMK-PLTs and PB-PLTs. y axis indicates relative mean fluorescence intensity (MFI) calculated as agonist minus no agonist. The MFI of no agonist was 1.0 in individual samples. Thrombin (1 U/mL) or ADP (20 μM)/TRAP (100 μM) was the agonist. Results are expressed as mean ± SEM; n = 9 for iMK-PLTs, n = 6 for PB-PLTs. *p < 0.05; **p < 0.01; ***p < 0.001.
(F) iMK-PLTs and PB-PLTs were spread on a fibrinogen surface. Adherent PLTs were immunostained with CD41 and α-tubulin antibodies. Scale bar, 10 μm.
(G) Pictures of clot retraction. PLT-depleted human plasma was added to the iMK-PLTs and PB-PLTs. Thrombin was then added to the suspensions to induce clot formation and retraction.
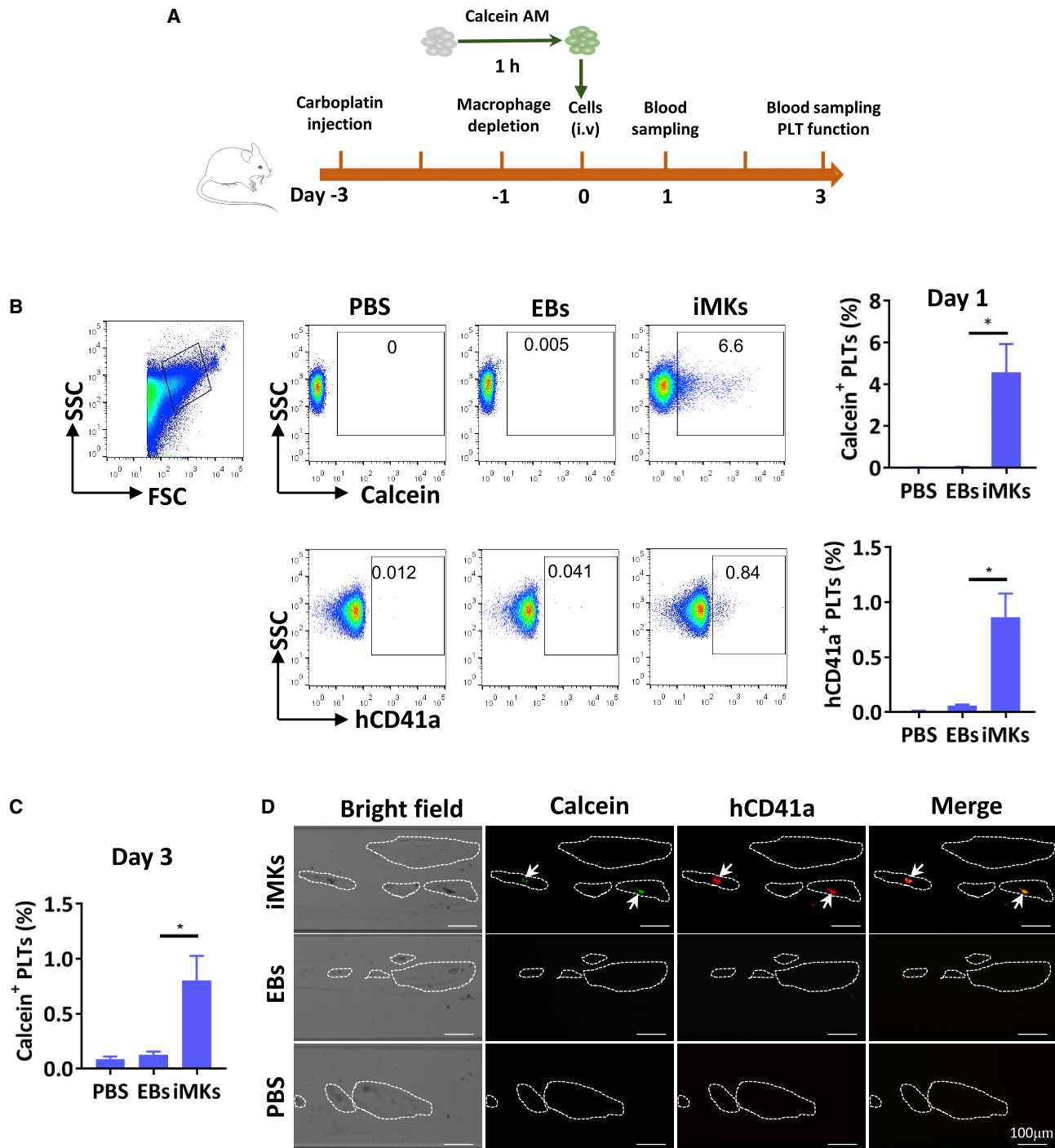
Figure 4. Induced megakaryocytes (iMKs) produced functional PLTs *in vivo*

(A) Diagram of the strategy used to evaluate PLT production by iMKs *in vivo*.

(B) Percentages of calcein⁺ and hCD41a⁺ anucleate PLT-sized cells in the mouse PB after 1 day of transfusion. Results are expressed as mean ± SEM; n = 2 for PBS, n = 3 for EBs, n = 6 for iMKs. *p < 0.05.

(C) Percentages of calcein⁺ anucleate PLT-sized cells in the mouse PB after 3 days of transfusion. Results are expressed as mean ± SEM; n = 2 for PBS, n = 3 for EBs, n = 5 for iMKs. *p < 0.05.

(D) Analysis of PLT adhesion and aggregation under controlled flow. Blood samples were collected from mice on 3 days after transfusion. Thrombi identified using bright field images are delineated. Calcein⁺ PLTs fluorescing in green, hCD41a antibody fluorescing in red. Scale bar, 100 μm.
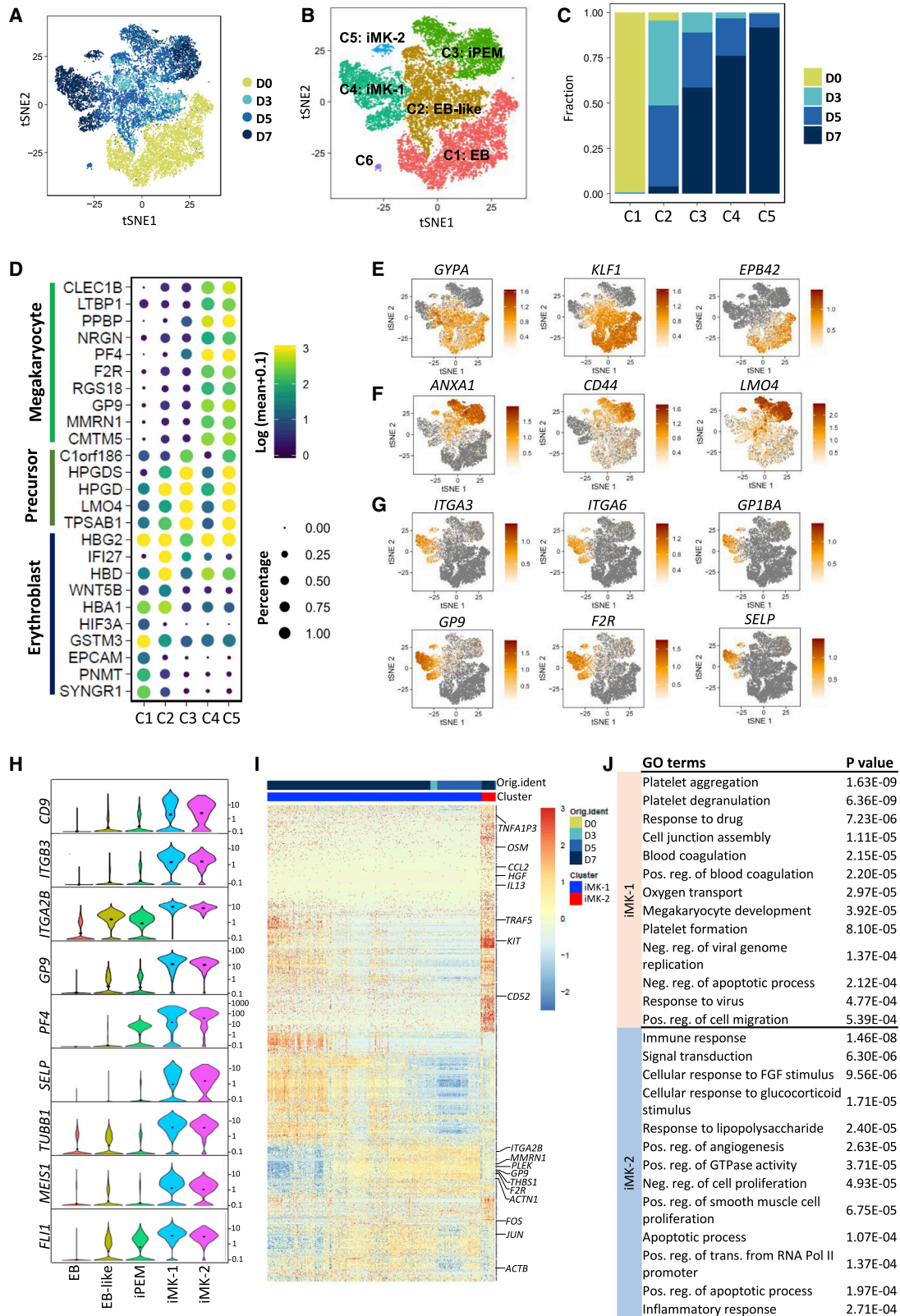
different supermodules according to their co-expression levels (Figure 6D). Supermodule 1 was enriched with erythroid gene sets, including *EPB42*, *HBA2*, and *AHSP*, which exhibited GO terms including "oxygen transport" and "response to hypoxia" (Figures 6E, 6F, and S6B). Supermodule 2 was enriched with megakaryocytic genes, such as *FLI1*, *PPBP*, *PF4*, *GP9*, *TUBB1*, and *THBS1*, which were associated with the functions "PLT degranulation" and "PLT activation" (Figures 6E, 6F, and S6B). MK-featured genes significantly increased over time and included *GP9*, *PF4*, *PPBP*, and *SELP* (Figures 6E and S6C). Supermodule 3 was enriched with genes related to cell division, such as *MKI67* and *CDK1*, which decreased in the late stage of pseudotime (Figures 6E and S6B). The GO terms related to the "interferon-gamma-mediated signal pathway" and "defense response to virus" were enriched in Supermodule 4 (Figure 6F). Representative genes, such as *MX1* and *IFTIM3*, exhibited transient increase and then downregulated expression patterns over the pseudotime trajectory (Figure 6E), indicating the existence of a special intermediate state of the reprogrammed cells under 4M induction. Notably, iPEMs showed high expression of *MX1* and *IFTIM3* as well as the TF gene *LMO4* (Figures 5F and S6D), which was reported to be required for definitive hematopoiesis in zebrafish (Meier et al., 2006). The TF network analysis further illustrated that immune response-related TFs such as *PARP12*, *SP110*, and interferon regulatory factors (*IRF1*, *IRF7*, and *IRF9*) were enriched in Supermodule 4. Moreover, Supermodule 1 exhibited expression of TFs essential for erythropoiesis, such as *KLF1* and *MYB*. In contrast, Supermodule 2 exhibited expression of TFs associated with megakaryopoiesis, such as *FLI1*, *MEIS1*, *PLEK*, and *NFIB* (Figure 6G). Together, these results dissected the sequential molecular progression that led to the successful reprogramming of EBs to MKs and revealed an intermediate state of iPEMs during the reprogramming pathway.

4M cocktail induces reprogramming of EBs to iMKs via chromatin remodeling

To understand how 4M reorganizes the chromatin architecture during the conversion of EBs to iMKs, we performed ATAC-seq on EBs (D0) and reprogrammed cells on D3, D5, and D7. The individual peaks were compared between D0 and D7 and divided into two categories: closed on D0 but open on D7 (CO) and open on D0 but closed on D7 (OC). Notably, 4M induction profoundly closed and opened many loci from D3 to D7 (Figure 7A). We then divided the CO and OC peaks into three subgroups individually to demonstrate the progression of chromatin accessibility dynamics (Figure 7B). Counting these peaks showed that OC1 ranked highest, suggesting that successful closing of chromatin loci dominated the early reprogramming process (Figure 7C).

The OC peaks tended to be widely distributed among the promoter, intron, and intergenic regions. Besides, more than 50% of the CO peaks were localized in the intergenic and intron regions (Figure 7D). These data indicated that the 4M cocktail induced genome-wide chromatin remodeling during reprogramming.

To gain mechanistic insight into the 4M-induced TF regulation dynamics at the chromatin level, we performed motif analysis on the relevant CO and OC loci. The binding motif for the zinc finger TF family, including KLF1 and KLF3-6, was highly enriched in OC1 and OC2 (Figure 7E), indicating that erythroid master regulators had a closed chromatin status in reprogrammed cells after 4M induction. Notably, the CO loci contained binding motifs for a set of hematopoietic stem cell and MK-associated TFs, including ERG, FLI1, GABPA, and RUNX1, distributed in CO1–3 (Figure 7E), indicating chromatin-level reprogramming by 4M and orchestration of hematopoiesis and MK cell fate transition by these TFs.

To explore the reprogramming mechanism of 4M from EBs to iMKs, we analyzed the chromatin status of key TFs during reprogramming. The master TF genes for erythroid development, including *MYB* and *KLF1*, exhibited profoundly reduced chromatin opening signals from D3 to D5 and the lowest opening signals on D7 compared to those on D0 (Figure 7F). Consistently, the scRNA-seq data revealed that the expression of these two TF genes gradually decreased along the reprogramming path (Figures 7G and S6D). Erythroid-characteristic genes, such as *HBB* and *EPB42*, also showed similarly lower opening levels and reduced expression levels during reprogramming, supporting that erythropoiesis was significantly inhibited by 4M (Figures S7A and S7B). In contrast, increased chromatin accessibility signals were observed in critical TF genes for megakaryopoiesis, including in *FLI1* and *MEIS1* and in MK-featured genes such as *PF4*, *THBS1*, and *SELP* (Figures 7H and S7C). Notably, the increased chromatin accessibility of these genes was correlated with their expression levels along pseudotime (Figures 7I and S7D), indicating successful MK fate conversion by 4M. Taken together, our data suggest that the reprogramming mechanism by 4M might involve decreasing the chromatin accessibility of erythroid essential TF genes and opening of the regulatory regions of hematopoietic and MK-crucial TF genes, subsequently driving MK fate specification.

DISCUSSION

In this study, we first reported that the 4M combination could rapidly and efficiently convert CB EBs into MK-like cells. The iMKs possessed critical characteristics of MKs, including CD41a and CD42b surface marker expression, DNA ploidy, and typical MK organelles. Also, the iMKs exhibited the

---

Figure 5. High-resolution dissection of 4M reprogramming from EBs to iMKs using scRNA-seq
(A) t-distributed stochastic neighbor embedding (t-SNE) projection of all individual cells during the reprogramming process, colored by the indicated time points.
(B) t-SNE plot showing six heterogeneous clusters of all individual cells collected on days 0, 3, 5, and 7.
(C) Stacked bar chart showing the percentage of cells at different time points within distinct clusters.
(D) Heatmap showing the expression of the top 5 marker genes in each cluster.
(E) Expression of selected erythroid marker genes (*GYPA*, *KLF1*, and *EPB42*) in all cells.
(F) Expression of selected precursor-associated marker genes (*ANXA1*, *CD44*, and *LMO4*) in all cells.
(G) Expression of selected megakaryocytic marker genes (*ITGA3*, *ITGA6*, *GP1BA*, *GP9*, *F2R*, and *SELP*) in all cells.
(H) Violin plot of typical megakaryocytic gene expressions in the five cell clusters.
(I) Heatmap showing differentially expressed genes between iMK-1 and iMK-2.
(J) Enriched major Gene Ontology terms for differentially expressed genes between iMK-1 and iMK-2.
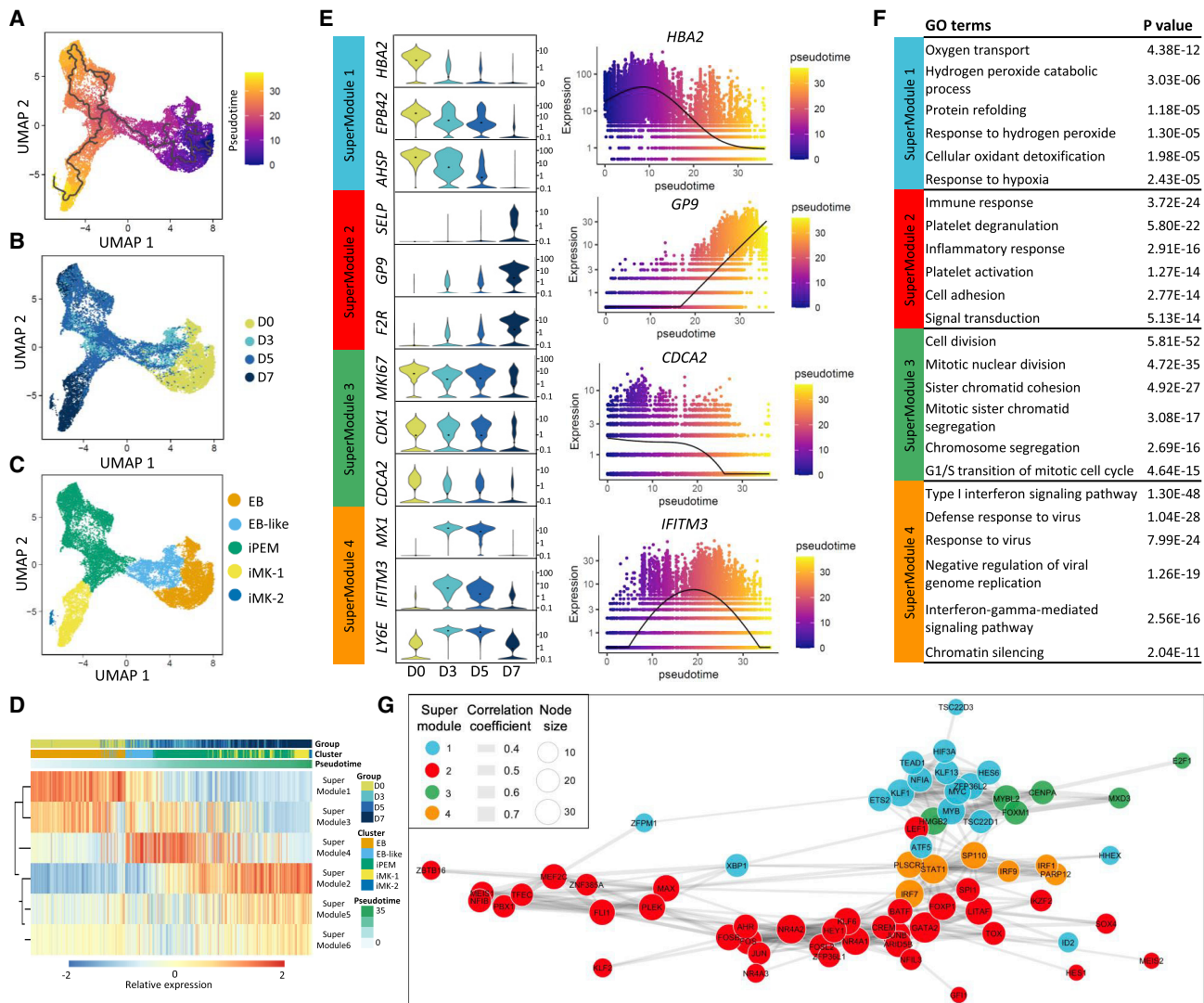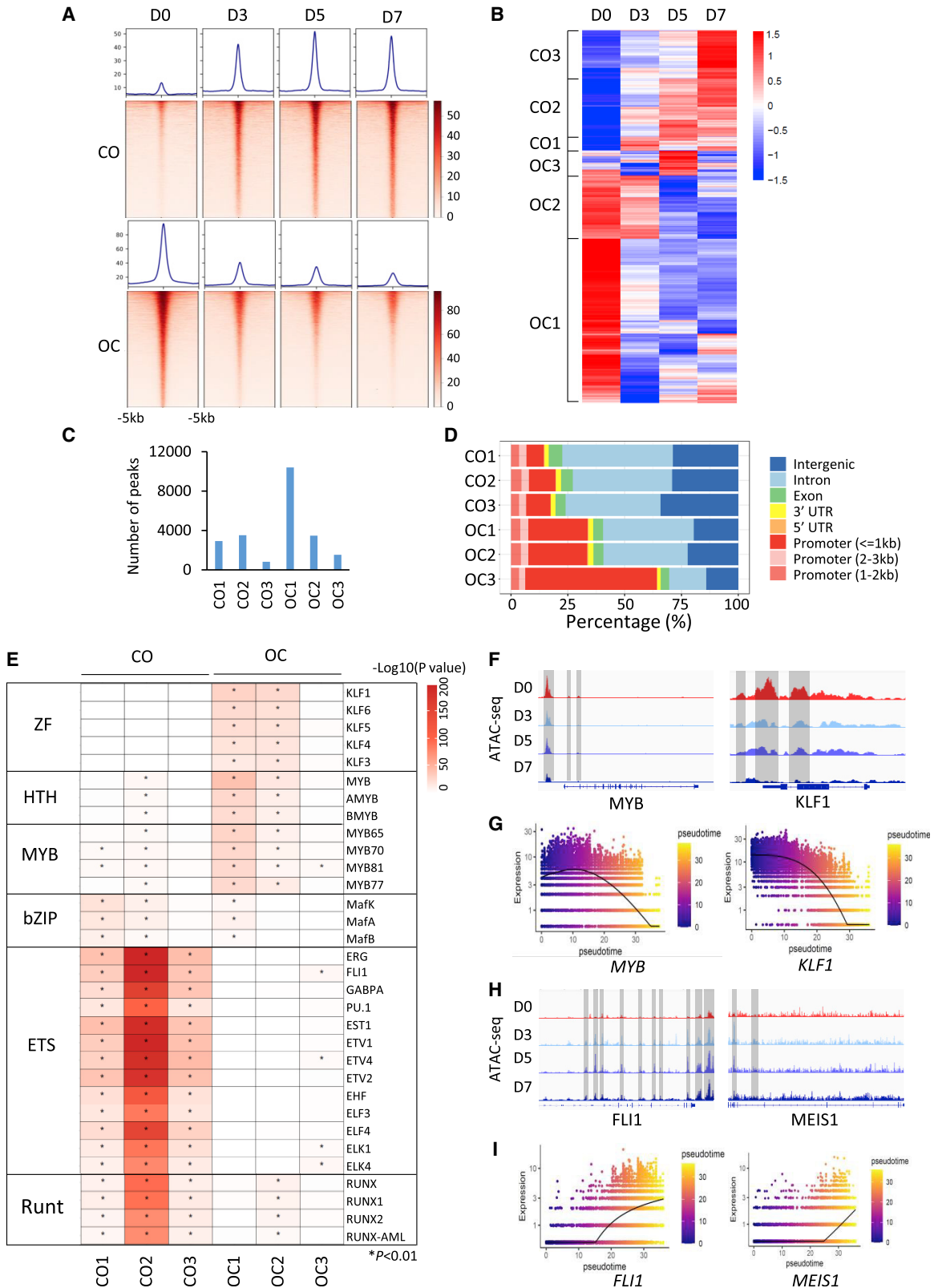
Figure 6. Reconstruction of chemical reprogramming trajectory in a pseudotime manner

(A) Pseudotime analysis of all single cells throughout chemical reprogramming.

(B) Uniform manifold approximation and projection (UMAP) plot of all individual cells during the reprogramming process, colored by indicated time points.

(C) UMAP projection of cell clusters along the inferred pseudotime axis.

(D) Heatmap of pseudotime-dependent genes along the inferred pseudotime axis (hierarchically cataloged into six supermodules).

(E) Violin plots of representative genes in each gene supermodule (left panel). Expression dynamics of representative genes in each gene supermodule along the inferred pseudotime axis (right panel).

(F) Representative Gene Ontology terms enriched in each gene supermodule.

(G) Correlation network of significant transcription factors (TFs) expressed in each gene module in (D). Node colors indicate different gene modules; line thickness indicates correlation coefficient, and only edges with adjusted p value < 0.05 and correlation coefficient >0.3 are shown; circle size indicates the number of edges that are incident to the node.

capabilities of differentiating into proplatelets and producing functional PLTs *in vitro*. After being transfused into thrombocytopenic mice, the iMKs released vital PLTs *in vivo*, which could participate in thrombi formation. In-depth scRNA-seq analysis demonstrated that the conversion of EBs to iMKs underwent a bipotent PEM intermediate.

Several studies indicated that the initial cells are critical for simplifying the reprogramming protocol. For example, mouse 3T3-L1 (a preadipocyte cell line) and human adipose-derived mesenchymal stem cell lines are relatively easy to convert

into MKs (Matsubara et al., 2010; Tozawa et al., 2018). However, it remains challenging to identify suitable seed cells and develop a simple reprogramming method to ensure high efficiency of conversion into MKs from special seed cells. The CB contains abundant EBs, and large numbers of EBs can be obtained through *in vitro* expansion (Fouquet et al., 2021; Liu et al., 2021b). In addition, the ontological link between EBs and MKs may help to find a simple reprogramming method for conversion of CB-derived EBs into functional MKs.

A (D0, D3, D5, D7 panels for CO and OC)

B (heatmap with CO3, CO2, CO1, OC3, OC2, OC1 across D0, D3, D5, D7)

C Number of peaks bar chart (CO1, CO2, CO3, OC1, OC2, OC3)

D Percentage (%) stacked bar chart with legend:
- Intergenic
- Intron
- Exon
- 3' UTR
- 5' UTR
- Promoter (<=1kb)
- Promoter (2-3kb)
- Promoter (1-2kb)

E -Log10(P value)

	CO			OC			
ZF				*	*		KLF1
				*	*		KLF6
				*	*		KLF5
				*	*		KLF4
				*	*		KLF3
HTH		*		*	*		MYB
				*	*		AMYB
		*		*	*		BMYB
MYB		*		*	*		MYB65
	*	*		*	*		MYB70
	*	*		*	*	*	MYB81
		*		*	*		MYB77
bZIP	*	*		*			MafK
	*	*		*			MafA
	*	*		*			MafB
ETS	*	*	*				ERG
	*	*	*			*	FLI1
	*	*	*				GABPA
	*	*	*				PU.1
	*	*	*				EST1
	*	*	*				ETV1
	*	*	*			*	ETV4
	*	*	*				ETV2
	*	*	*				EHF
	*	*	*				ELF3
	*	*	*				ELF4
	*	*	*			*	ELK1
	*	*	*			*	ELK4
Runt	*	*	*		*		RUNX
	*	*	*		*		RUNX1
	*	*	*		*		RUNX2
	*	*	*		*		RUNX-AML

*P<0.01

CO1 CO2 CO3 OC1 OC2 OC3

F ATAC-seq (D0, D3, D5, D7) — MYB, KLF1

G Expression vs pseudotime — *MYB*, *KLF1*

H ATAC-seq (D0, D3, D5, D7) — FLI1, MEIS1

I Expression vs pseudotime — *FLI1*, *MEIS1*

(legend on next page)

Introduction of exogenous TFs into EBs for MK fate transition has been proven feasible. Nevertheless, given that TF-induced reprogramming methods are associated with safety issues in subsequent clinical applications, chemical reprogramming techniques would be a better choice for generating therapeutic MKs and PLTs. Epigenetics-regulated and signal-pathway-related small molecules are often used to initiate cell fate conversion among different cell types (Cao et al., 2016; Li et al., 2015; Wang et al., 2016; Zhang et al., 2015; Zhao et al., 2018). Thus, we screened a pool of different epigenetics- and signal-pathway-regulated chemicals according to the appearance of the MK-specific surface markers CD41a and CD42b. We discovered a combination of 4M that can efficiently reprogram EBs into MKs in the culture medium with cytokines. Among them, PD0325091 (a pan MEK1/2 inhibitor) was crucial for cell fate conversion from EBs toward MKs (Figure S1D). Accumulating evidence indicated that the MEK1/2 downstream signal molecules ERK1 and ERK2 have distinct biological functions (Göke et al., 2013). It might be meaningful to determine the specific roles of each ERK isoform and decipher their downstream targets during reprogramming.

Recent reports suggested that MKs are heterogeneous and immune-related MKs are present in the fetal liver (Wang et al., 2020) and lung (Lefrançais et al., 2017). We found that iMK-1 constituted the majority of $CD41a^+CD42b^+$ cells on days 7 and 14, indicating that our culture system is beneficial for the generation of thrombopoiesis-biased MKs. By dissecting sequential molecular events, we revealed a dynamic transition from the erythroid characteristic gene signature to MK-like program. Upregulation of MK development-associated TF networks by 4M, including *FLI1* and *MEIS1*, led human CB EBs to acquire the MK cell fate. The reprogramming trajectory in a pseudotime manner of 4M reprogramming from EBs to iMKs revealed that the initial EBs were pushed into an iPEM intermediate status and then pulled towards the MK cell fate. PEMs with erythroid and megakaryocytic cell differentiation potential have been identified as a rare cell population in the normal BM (Vannucchi et al., 2000). A subsequent study indicated that PEM differs from MEP and exhibits a lower proliferation potential than MEP, which may be downstream of MEP under the steady state or erythroid stress in a mouse model (Sanchez et al., 2006). This PEM population was identified in expansion cultures of human CB $CD34^+$ cells and exists at very low levels in unexpanded CB (Belay et al., 2015). Similarly, iPEMs were identified in our 4M-induced MK reprogramming system initiated from CB EBs and demonstrated erythroid and megakaryocytic cell differentiation potential (Figure S5E). In addition, iPEMs reprogrammed from EBs showed higher expression levels of the glucocorticoid receptor (GR) than EBs or iMKs (Figure S5F). GO analysis of iPEMs demon-

strated that glucocorticoid-related gene sets were significantly enriched (Figure S5G), indicating that glucocorticoids may play an important role in iPEM production and maintenance (Lee et al., 2015; Varricchio et al., 2012). Accumulating evidence indicated that microenvironmental cues can program or reprogram cell fate by regulating intrinsic signaling pathways, epigenetic states, and gene expression (Bloom and Zaman, 2014; Chen et al., 2018; Song et al., 2020). In this reprogramming system, we used a small-molecule cocktail to regulate the intracellular epigenetic state. 4M induced genome-wide chromatin remodeling during reprogramming, particularly by opening a series of MK-related TF and functional gene loci (Figures 7H and S7), enabling intracellular signals and key TFs to access the regulatory elements in iPEM- and MK-related genes (Figure 7E). The combined effect of 4M with hematopoietic cytokines led to complicated signal cascade alterations in iPEMs, including PI3K/AKT and JAK/STAT signaling (Figure S5H), which may collectively drive reprogramming. Our findings offer a high-resolution dissection of cell fate dynamics during chemical reprogramming and shed light on mechanistic insights into the cell fate conversion nature of iMKs from EBs.

To further promote the differentiation and maturation of iMKs after chemical reprogramming, the induced cells on day 7 were then cultured in megakaryocytic specification medium with cytokines. Notably, iMKs with high expression of the CD41a and CD42b surface markers increased remarkably on day 14, which showed similar phenotype and function as BM-MKs. However, the expression levels of FOG1 and THBS1 in iMKs and the ploidy levels of iMKs were relatively lower than natural MKs. Further enhancement of the polyploidization or terminal maturation of iMKs could improve the yield of PLTs *in vitro* (Mazzi et al., 2018). We found that iMK-PLTs exhibited hyporesponsiveness to thrombin stimulation, which might be related to the developmental differences between iMK-PLTs and natural PLTs. Similarly, neonatal PLTs were found to be hyporeactive to agonists (Tesfamariam, 2017). In addition, the preactivation of *in-vitro*-generated PLTs might be one of the main reasons that affect the agonist responsiveness of induced PLTs (Wang et al., 2015). In the future, proper *ex vivo* culture conditions need to be introduced to produce PLTs with better functionality. In recent years, infusion of MKs has become an alternative therapeutic approach for thrombocytopenic patients. By employing animal experiments and *in vitro* PRP adhesion and aggregation under controlled flow (Fuentes et al., 2013; Moreau et al., 2016), we showed that iMKs could indeed produce PLTs *in vivo*. We also showed that the PLTs derived from iMKs were functional and could participate in thrombi formation.

Figure 7. ATAC-seq reveals chromatin dynamics during reprogramming
(A) Heatmap and pileup of ATAC-seq signal. The heatmap and pileups are centered on the ATAC-seq peak (upstream 5 kb and downstream 5 kb of the peaks).
(B) Chromatin loci arranged into groups according to time and status being closed or opened as closed-to-open (CO) or open-to-closed (OC).
(C) The number of peaks defined in CO and OC.
(D) Peak distribution across genomic features for the OC/CO groups.
(E) TF motifs significantly enriched at least >2.0-fold for CO/OC/PO categories of ATAC-seq peaks. TF families are indicated on the right of the heatmap. *p < 0.01.
(F) Selected genomic views of ATAC-seq data. MYB (chr6:135,494,990–135,544,942), KLF1 (chr19:12,994,363–12,998,966). OC loci are marked with a gray box.
(G) The expression dynamics of *MYB* and *KLF1* along the inferred pseudotime axis.
(H) Selected genomic views of ATAC-seq data. FLI1 (chr11:128,570,182–128,697,127), MEIS1 (chr2:66,661,922–66,799,283). CO loci are marked with a gray box.
(I) Expression dynamics of *FLI1* and *MEIS1* along the inferred pseudotime axis.

Given that infused MKs are distributed in several tissues, including BM, lung, and spleen, and that these cells might release PLTs for several days (Fuentes et al., 2010; Patel et al., 2019; Wang et al., 2015), it is difficult to accurately calculate human PLTs in a mouse model. Thus, we analyzed the PLT numbers generated by iMK *in vitro*. One CB unit (∼100 mL) from public CB banks contains ∼1.0 ×10^9 total nucleated cells or ∼4.36×10^8 mononuclear cells (Hollands, 2012; Pamphilon et al., 2011; Pope et al., 2012). Theoretically, it is possible to obtain ∼6×10^8 EBs from one CB unit after 7-day expansion, subsequently generate 3.58–6.28×10^9 iMKs after 2-phase induction, and finally generate 0.36–1.22×10^{11} PLTs based on our small-scale iMK and PLT manufacturing data. The yield of induced PLTs from one CB sample was less than a unit of single-donor PLTs (2–3 × 10^{11}) (Malodan et al., 2022; Perez Aliaga et al., 2021). Further studies are needed to improve the yield of PLTs from iMKs by increasing the expansion capacity of iMKs and employing bioreactors (Ito et al., 2018).

In summary, we successfully generated human iMKs and PLTs from umbilical CB EBs using a chemical reprogramming strategy with a 4M combination and subsequent specification-phase culture. The iMKs resembled natural MKs in phenotype and function, releasing functional PLTs both *in vivo* and *in vitro*. This small-molecule reprogramming strategy is rapid and efficient, and it circumvents the pluripotent stem cell or hematopoietic stem/progenitor cell reprogramming path. Thus, chemical reprogramming of EBs to iMKs provides a simple and efficient path for generating clinically transfusible MKs and PLTs to reduce the risk of hemorrhage and death in patients with severe thrombocytopenia.

Limitations of the study

Although our chemical reprogramming protocol converts human CB EBs into iMKs, the yield of PLTs is relatively low. Further studies are needed to improve iMK maturation and PLT release by optimizing culture conditions and employing bioreactors. In addition, comparison of tissue distribution and half-life of iMK-PLTs with human natural MKs and PLTs *in vivo* awaits future exploration. Finally, it is still difficult to decipher the reprogramming mechanism clearly. Identification of a core small molecule that modulates cell fate transition may help to understand the reprogramming mechanism and increase the reprogramming efficiency.

STAR★METHODS

Detailed methods are provided in the online version of this paper and include the following:

- KEY RESOURCES TABLE
- RESOURCE AVAILABILITY
  - Lead contact
  - Materials availability
  - Data and code availability
- EXPERIMENTAL MODEL AND SUBJECT DETAILS
  - Animals
  - Human subjects
- METHOD DETAILS
  - Purification of human CB-derived erythroblasts
  - Conversion of erythroblasts to iMKs
  - Proplatelet formation and platelet production

- PF4 reporter lentivirus transduction
- Flow cytometry
- Morphologic analysis
- Immunofluorescence staining
- Quantitative real-time PCR analyses
- Measurement of THBS1 and PF4
- Transmission electron microscopy
- Ploidy analysis
- MK isolation from human BM
- Preparation of human PB-PLTs and iMK-PLTs
- Flow cytometric analysis of platelet activation
- Spreading assay
- Clot formation and retraction
- *In vivo* MK infusion experiments
- Analysis of platelet adhesion and aggregation under controlled flow
- Karyotype analysis
- scRNA-seq
- Primary process and quality control of scRNA-seq data
- Visualization and clustering
- Trajectory analysis
- Cell cycle regression
- GO enrichment analysis
- Cell type correlation analysis
- TF network construction
- ATAC-seq
- ATAC-seq bioinformatics analysis
- QUANTIFICATION AND STATISTICAL ANALYSIS

AUTHOR CONTRIBUTIONS

J.Q., Y.-H.L., and X.P. designed the study. J.Q. and J.J. conducted the experiments, analyzed data, and prepared the draft manuscript. J.Z. performed the bioinformatics analysis. B.Z., J.L., X.L., S.W., M.Z., and Y.L. helped with the *in vivo* transfusion experiments. Z.F. assisted with the flow cytometry analysis. L.H, L.C., and W.Y. provided technical or material support. J.Q. and Y.-H.L. analyzed data and wrote the manuscript. All authors have read and approved the manuscript.

REFERENCES

Ang, Y.-S., Gaspar-Maia, A., Lemischka, I.R., and Bernstein, E. (2011). Stem cells and reprogramming: breaking the epigenetic barrier? Trends Pharmacol. Sci. *32*, 394–401.

Belay, E., Miller, C.P., Kortum, A.N., Torok-Storb, B., Blau, C.A., and Emery, D.W. (2015). A hyperactive Mpl-based cell growth switch drives macrophage-associated erythropoiesis through an erythroid-megakaryocytic precursor. Blood *125*, 1025–1033.

Bloom, A.B., and Zaman, M.H. (2014). Influence of the microenvironment on cell fate determination and migration. Physiol. Genom. *46*, 309–314.

Buenrostro, J.D., Wu, B., Chang, H.Y., and Greenleaf, W.J. (2015). ATAC-seq: a method for assaying chromatin accessibility genome-wide. Curr. Protoc. Mol. Biol. *109*, 21.29.1–21.29.9.

Cao, J., Spielmann, M., Qiu, X., Huang, X., Ibrahim, D.M., Hill, A.J., Zhang, F., Mundlos, S., Christiansen, L., Steemers, F.J., et al. (2019). The single-cell transcriptional landscape of mammalian organogenesis. Nature *566*, 496–502.

Cao, N., Huang, Y., Zheng, J., Spencer, C.I., Zhang, Y., Fu, J.D., Nie, B., Xie, M., Zhang, M., Wang, H., et al. (2016). Conversion of human fibroblasts into functional cardiomyocytes by small molecules. Science *352*, 1216–1220.

Capellera-Garcia, S., Pulecio, J., Dhulipala, K., Siva, K., Rayon-Estrada, V., Singbrant, S., Sommarin, M.N.E., Walkley, C.R., Soneji, S., Karlsson, G., et al. (2016). Defining the minimal factors required for erythropoiesis through direct lineage conversion. Cell Rep. *15*, 2550–2562.

Chen, X., Li, J., Huang, Y., Liu, P., and Fan, Y. (2018). Insoluble microenvironment facilitating the generation and maintenance of pluripotency. Tissue Eng. Part B Rev. *24*, 267–278.

Cobaleda, C., Jochum, W., and Busslinger, M. (2007). Conversion of mature B cells into T cells by dedifferentiation to uncommitted progenitors. Nature *449*, 473–477.

Corces, M.R., Trevino, A.E., Hamilton, E.G., Greenside, P.G., Sinnott-Armstrong, N.A., Vesuna, S., Satpathy, A.T., Rubin, A.J., Montine, K.S., Wu, B., et al. (2017). An improved ATAC-seq protocol reduces background and enables interrogation of frozen tissues. Nat. Methods *14*, 959–962.

Ebrahimi, B. (2015). Reprogramming barriers and enhancers: strategies to enhance the efficiency and kinetics of induced pluripotency. Cell Regen. *4*, 10.

Eminli, S., Foudi, A., Stadtfeld, M., Maherali, N., Ahfeldt, T., Mostoslavsky, G., Hock, H., and Hochedlinger, K. (2009). Differentiation stage determines potential of hematopoietic cells for reprogramming into induced pluripotent stem cells. Nat. Genet. *41*, 968–976.

Fouquet, G., Thongsa-Ad, U., Lefevre, C., Rousseau, A., Tanhuad, N., Khongkla, E., Saengsawang, W., Anurathapan, U., Hongeng, S., Maciel, T.T., et al. (2021). Iron-loaded transferrin potentiates erythropoietin effects on erythroblast proliferation and survival: a novel role through transferrin receptors. Exp. Hematol. *99*, 12–20.e3.

Fu, Y., Huang, C., Xu, X., Gu, H., Ye, Y., Jiang, C., Qiu, Z., and Xie, X. (2015). Direct reprogramming of mouse fibroblasts into cardiomyocytes with chemical cocktails. Cell Res. *25*, 1013–1024.

Fuentes, E., Alarcón, M., Astudillo, L., Valenzuela, C., Gutiérrez, M., and Palomo, I. (2013). Protective mechanisms of guanosine from Solanum lycopersicum on agonist-induced platelet activation: role of sCD40L. Molecules *18*, 8120–8135.

Fuentes, R., Wang, Y., Hirsch, J., Wang, C., Rauova, L., Worthen, G.S., Kowalska, M.A., and Poncz, M. (2010). Infusion of mature megakaryocytes into mice yields functional platelets. J. Clin. Invest. *120*, 3917–3922.

Göke, J., Chan, Y.-S., Yan, J., Vingron, M., and Ng, H.-H. (2013). Genome-wide kinase-chromatin interactions reveal the regulatory network of ERK signaling in human embryonic stem cells. Mol. Cell *50*, 844–855.

Guan, X., Qin, M., Zhang, Y., Wang, Y., Shen, B., Ren, Z., Ding, X., Dai, W., and Jiang, Y. (2017). Safety and efficacy of megakaryocytes induced from hematopoietic stem cells in murine and nonhuman primate models. Stem Cells Transl. Med. *6*, 897–909.

Haghverdi, L., Lun, A.T.L., Morgan, M.D., and Marioni, J.C. (2018). Batch effects in single-cell RNA-sequencing data are corrected by matching mutual nearest neighbors. Nat. Biotechnol. *36*, 421–427.

Heinz, S., Benner, C., Spann, N., Bertolino, E., Lin, Y.C., Laslo, P., Cheng, J.X., Murre, C., Singh, H., and Glass, C.K. (2010). Simple combinations of lineage-determining transcription factors prime cis-regulatory elements required for macrophage and B cell identities. Mol. Cell *38*, 576–589.

Hochedlinger, K., and Plath, K. (2009). Epigenetic reprogramming and induced pluripotency. Development *136*, 509–523.

Hollands, P. (2012). 5 - Basic principles of cord blood stem cells. In Progenitor and Stem Cell Technologies and Therapies, A. Atala, ed. (Woodhead Publishing), pp. 77–99.

Hou, P., Li, Y., Zhang, X., Liu, C., Guan, J., Li, H., Zhao, T., Ye, J., Yang, W., Liu, K., et al. (2013). Pluripotent stem cells induced from mouse somatic cells by small-molecule compounds. Science *341*, 651–654.

Hu, W., Qiu, B., Guan, W., Wang, Q., Wang, M., Li, W., Gao, L., Shen, L., Huang, Y., Xie, G., et al. (2015). Direct conversion of normal and Alzheimer's disease human fibroblasts into neuronal cells by small molecules. Cell Stem Cell *17*, 204–212.

Hu, Z., and Yang, Y.-G. (2012). Full reconstitution of human platelets in humanized mice after macrophage depletion. Blood *120*, 1713–1716.

Huang, D.W., Sherman, B.T., and Lempicki, R.A. (2009). Systematic and integrative analysis of large gene lists using DAVID bioinformatics resources. Nat. Protoc. *4*, 44–57.

Huangfu, D., Osafune, K., Maehr, R., Guo, W., Eijkelenboom, A., Chen, S., Muhlestein, W., and Melton, D.A. (2008). Induction of pluripotent stem cells from primary human fibroblasts with only Oct4 and Sox2. Nat. Biotechnol. *26*, 1269–1275.

Ito, Y., Nakamura, S., Sugimoto, N., Shigemori, T., Kato, Y., Ohno, M., Sakuma, S., Ito, K., Kumon, H., Hirose, H., et al. (2018). Turbulence activates platelet biogenesis to enable clinical scale ex vivo production. Cell *174*, 636–648.e18.

Jiang, J., Qin, J., Li, J., Lin, X., Zhang, B., Fan, Z., He, L., Zeng, Q., Yue, W., Zheng, M., et al. (2022). Ricolinostat promotes the generation of megakaryocyte progenitors from human hematopoietic stem and progenitor cells. Stem Cell Res. Ther. *13*, 54.

Klimchenko, O., Mori, M., DiStefano, A., Langlois, T., Larbret, F., Lecluse, Y., Feraud, O., Vainchenker, W., Norol, F., and Debili, N. (2009). A common bipotent progenitor generates the erythroid and megakaryocyte lineages in embryonic stem cell-derived primitive hematopoiesis. Blood *114*, 1506–1517.

Kumar, N.D., Tomar, V., Singh, B., and Kela, K. (2000). Platelet transfusion practice during dengue fever epidemic. Indian J. Pathol. Microbiol. *43*, 55–60.

Lee, H.Y., Gao, X., Barrasa, M.I., Li, H., Elmes, R.R., Peters, L.L., and Lodish, H.F. (2015). PPAR-alpha and glucocorticoid receptor synergize to promote erythroid progenitor self-renewal. Nature *522*, 474–477.

Lefrançais, E., Ortiz-Muñoz, G., Caudrillier, A., Mallavia, B., Liu, F., Sayah, D.M., Thornton, E.E., Headley, M.B., David, T., Coughlin, S.R., et al. (2017). The lung is a site of platelet biogenesis and a reservoir for haematopoietic progenitors. Nature *544*, 105–109.

Li, X., Zuo, X., Jing, J., Ma, Y., Wang, J., Liu, D., Zhu, J., Du, X., Xiong, L., Du, Y., et al. (2015). Small-molecule-driven direct reprogramming of mouse fibroblasts into functional neurons. Cell Stem Cell *17*, 195–203.

Lin, T., Ambasudhan, R., Yuan, X., Li, W., Hilcove, S., Abujarour, R., Lin, X., Hahm, H.S., Hao, E., Hayek, A., and Ding, S. (2009). A chemical platform for improved induction of human iPSCs. Nat. Methods *6*, 805–808.

Liu, S., Wu, M., Lancelot, M., Deng, J., Gao, Y., Roback, J.D., Chen, T., and Cheng, L. (2021b). BMI1 enables extensive expansion of functional erythroblasts from human peripheral blood mononuclear cells. Mol. Ther. *29*, 1918–1932.

Macosko, E.Z., Basu, A., Satija, R., Nemesh, J., Shekhar, K., Goldman, M., Tirosh, I., Bialas, A.R., Kamitaki, N., Martersteck, E.M., et al. (2015). Highly parallel genome-wide expression profiling of individual cells using nanoliter droplets. Cell *161*, 1202–1214.

Magallon, J., Chen, J., Rabbani, L., Dangas, G., Yang, J., Bussel, J., and Diacovo, T. (2011). Humanized mouse model of thrombosis is predictive of the clinical efficacy of antiplatelet agents. Circulation *123*, 319–326.

Mahato, B., Kaya, K.D., Fan, Y., Sumien, N., Shetty, R.A., Zhang, W., Davis, D., Mock, T., Batabyal, S., Ni, A., et al. (2020). Pharmacologic fibroblast reprogramming into photoreceptors restores vision. Nature *581*, 83–88.

Malodan, R., Murugesan, M., and Nayanar, S.K. (2022). Predicting donor-related factors for high platelet yield donations by classification and regression tree analysis. Hematol. Transfus. Cell Ther.

Matsubara, Y., Suzuki, H., Ikeda, Y., and Murata, M. (2010). Generation of megakaryocytes and platelets from preadipocyte cell line 3T3-L1, but not the parent cell line 3T3, in vitro. Biochem. Biophys. Res. Commun. *402*, 796–800.

Matsunaga, T., Tanaka, I., Kobune, M., Kawano, Y., Tanaka, M., Kuribayashi, K., Iyama, S., Sato, T., Sato, Y., Takimoto, R., et al. (2006). Ex vivo large-scale generation of human platelets from cord blood CD34+Cells. Stem Cells *24*, 2877–2887.

Mazzi, S., Lordier, L., Debili, N., Raslova, H., and Vainchenker, W. (2018). Megakaryocyte and polyploidization. Exp. Hematol. *57*, 1–13.

Meier, N., Krpic, S., Rodriguez, P., Strouboulis, J., Monti, M., Krijgsveld, J., Gering, M., Patient, R., Hostert, A., and Grosveld, F. (2006). Novel binding partners of Ldb1 are required for haematopoietic development. Development *133*, 4913–4923.

Moreau, T., Evans, A.L., Vasquez, L., Tijssen, M.R., Yan, Y., Trotter, M.W., Howard, D., Colzani, M., Arumugam, M., Wu, W.H., et al. (2016). Large-scale production of megakaryocytes from human pluripotent stem cells by chemically defined forward programming. Nat. Commun. *7*, 11208.

Morris, S.A., and Daley, G.Q. (2013). A blueprint for engineering cell fate: current technologies to reprogram cell identity. Cell Res. *23*, 33–48.

Nakamura, S., Takayama, N., Hirata, S., Seo, H., Endo, H., Ochi, K., Fujita, K.i., Koike, T., Harimoto, K.i., Dohda, T., et al. (2014). Expandable megakaryocyte cell lines enable clinically applicable generation of platelets from human induced pluripotent stem cells. Cell Stem Cell *14*, 535–548.

Pamphilon, D., Curnow, E., Belfield, H., Reems, J.A., McMannis, J., Lecchi, L., Szczepiorkowski, Z., and McKenna, D. (2011). Storage characteristics of cord blood progenitor cells: report of a multicenter study by the cellular therapies team of the Biomedical Excellence for Safer Transfusion (BEST) collaborative. Transfusion *51*, 1284–1290.

Patel, A., Clementelli, C.M., Jarocha, D., Mosoyan, G., Else, C., Kintali, M., Fong, H., Tong, J., Gordon, R., Gillespie, V., et al. (2019). Pre-clinical development of a cryopreservable megakaryocytic cell product capable of sustained platelet production in mice. Transfusion *59*, 3698–3713.

Pérez Aliaga, A.I., Labata, G., Aranda, A., Cardoso, M., Puente, F., Domingo, J.M., and Garcés, C. (2021). Improvement of blood processing and safety by automation and pathogen reduction technology. Transfus. Med. Hemother. *48*, 290–297.

Polo, J.M., Liu, S., Figueroa, M.E., Kulalert, W., Eminli, S., Tan, K.Y., Apostolou, E., Stadtfeld, M., Li, Y., Shioda, T., et al. (2010). Cell type of origin influences the molecular and functional properties of mouse induced pluripotent stem cells. Nat. Biotechnol. *28*, 848–855.

Pope, B., Mitsakos, K., Bilgin, A., Hokin, B., and Grant, R. (2012). Predicting overall viability of cord blood harvests. Transfusion *52*, 1079–1085.

Psaila, B., Lyden, D., and Roberts, I. (2012). Megakaryocytes, malignancy and bone marrow vascular niches. J. Thromb. Haemost. *10*, 177–188.

Pulecio, J., Alejo-Valle, O., Capellera-Garcia, S., Vitaloni, M., Rio, P., Mejía-Ramírez, E., Caserta, I., Bueren, J.A., Flygare, J., and Raya, A. (2016). Direct conversion of fibroblasts to megakaryocyte progenitors. Cell Rep. *17*, 671–683.

Ramírez, F., Ryan, D.P., Grüning, B., Bhardwaj, V., Kilpert, F., Richter, A.S., Heyne, S., Dündar, F., and Manke, T. (2016). deepTools2: a next generation web server for deep-sequencing data analysis. Nucleic Acids Res. *44*, W160–W165.

Reems, J.A., Pineault, N., and Sun, S. (2010). In vitro megakaryocyte production and platelet biogenesis: state of the art. Transfus. Med. Rev. *24*, 33–43.

Robert, A., Cortin, V., Garnier, A., and Pineault, N. (2012). Megakaryocyte and platelet production from human cord blood stem cells. Methods Mol. Biol. *788*, 219–247.

Sanchez, M., Weissman, I.L., Pallavicini, M., Valeri, M., Guglielmelli, P., Vannucchi, A.M., Migliaccio, G., and Migliaccio, A.R. (2006). Differential amplification of murine bipotent megakaryocytic/erythroid progenitor and precursor cells during recovery from acute and chronic erythroid stress. Stem Cell. *24*, 337–348.

Shi, Y., Desponts, C., Do, J.T., Hahm, H.S., Schöler, H.R., and Ding, S. (2008). Induction of pluripotent stem cells from mouse embryonic fibroblasts by Oct4 and Klf4 with small-molecule compounds. Cell Stem Cell *3*, 568–574.

Siripin, D., Kheolamai, P., U-Pratya, Y., Supokawej, A., Wattanapanitch, M., Klincumhom, N., Laowtammathron, C., and Issaragrisil, S. (2015). Transdifferentiation of erythroblasts to megakaryocytes using FLI1 and ERG transcription factors. Thromb. Haemost. *114*, 593–602.

Song, Y., Soto, J., Chen, B., Yang, L., and Li, S. (2020). Cell engineering: Biophysical regulation of the nucleus. Biomaterials *234*, 119743.

Stallard, R. (1998). In The AGT Cytogenetics Laboratory Manual, 3rd ed, M. J Barch, T. Knutsen, and J.L. Spurbeck, eds. (Lippincott-Raven Publishers), p. 666.

Stroncek, D.F., and Rebulla, P. (2007). Platelet transfusions. Lancet *370*, 427–438.

Stuart, T., Butler, A., Hoffman, P., Hafemeister, C., Papalexi, E., Mauck, W.M., 3rd, Hao, Y., Stoeckius, M., Smibert, P., and Satija, R. (2019). Comprehensive integration of single-cell data. Cell *177*, 1888–1902.e21.

Stubbs, J.R., Homer, M.J., Silverman, T., and Cap, A.P. (2021). The current state of the platelet supply in the US and proposed options to decrease the risk of critical shortages. Transfusion *61*, 303–312.

Sun, S., Jin, C., Si, J., Lei, Y., Chen, K., Cui, Y., Liu, Z., Liu, J., Zhao, M., Zhang, X., et al. (2021). Single-cell analysis of ploidy and the transcriptome reveals functional and spatial divergency in murine megakaryopoiesis. Blood *138*, 1211–1224.

Takayama, N., Nishikii, H., Usui, J., Tsukui, H., Sawaguchi, A., Hiroyama, T., Eto, K., and Nakauchi, H. (2008). Generation of functional platelets from human embryonic stem cells in vitro via ES-sacs, VEGF-promoted structures that concentrate hematopoietic progenitors. Blood *111*, 5298–5306.

Tesfamariam, B. (2017). Distinct characteristics of neonatal platelet reactivity. Pharmacol. Res. *123*, 1–9.

Tirosh, I., Izar, B., Prakadan, S.M., Wadsworth, M.H., Treacy, D., Trombetta, J.J., Rotem, A., Rodman, C., Lian, C., Murphy, G., et al. (2016). Dissecting the multicellular ecosystem of metastatic melanoma by single-cell RNA-seq. Science *352*, 189–196.

Tozawa, K., Ono-Uruga, Y., Yazawa, M., Mori, T., Murata, M., Okamoto, S., Ikeda, Y., and Matsubara, Y. (2018). Unique megakaryocytes and platelets from novel human adipose-derived mesenchymal stem cell line. Blood.

Traag, V., A, Waltman, and van Eck, N., J (2019). From Louvain to Leiden: guaranteeing well-connected communities. Scientific Reports *9* (5233).

Ulich, T., del Castillo, J., Yin, S., Swift, S., Padilla, D., Senaldi, G., Bennett, L., Shutter, J., Bogenberger, J., and Sun, D. (1995). Megakaryocyte growth and development factor ameliorates carboplatin- induced thrombocytopenia in mice. Blood *86*, 971–976.

Vannucchi, A.M., Paoletti, F., Linari, S., Cellai, C., Caporale, R., Ferrini, P.R., Sanchez, M., Migliaccio, G., and Migliaccio, A.R. (2000). Identification and characterization of a bipotent (erythroid and megakaryocytic) cell precursor from the spleen of phenylhydrazine-treated mice. Blood *95*, 2559–2568.

Varricchio, L., Tirelli, V., Masselli, E., Ghinassi, B., Saha, N., Besmer, P., and Migliaccio, A.R. (2012). The expression of the glucocorticoid receptor in human erythroblasts is uniquely regulated by KIT ligand: implications for stress erythropoiesis. Stem Cells Dev. *21*, 2852–2865.

Wang, H., He, J., Xu, C., Chen, X., Yang, H., Shi, S., Liu, C., Zeng, Y., Wu, D., Bai, Z., et al. (2020). Decoding human megakaryocyte development. Cell Stem Cell *28*, 535–549.e8.

Wang, Y., Hayes, V., Jarocha, D., Sim, X., Harper, D.C., Fuentes, R., Sullivan, S.K., Gadue, P., Chou, S.T., Torok-Storb, B.J., et al. (2015). Comparative

analysis of human ex vivo-generated platelets vs megakaryocyte-generated platelets in mice: a cautionary tale. Blood 125, 3627–3636.

Wang, Y., Qin, J., Wang, S., Zhang, W., Duan, J., Zhang, J., Wang, X., Yan, F., Chang, M., Liu, X., et al. (2016). Conversion of human gastric epithelial cells to multipotent endodermal progenitors using defined small molecules. Cell Stem Cell 19, 449–461.

Xavier-Ferrucio, J., and Krause, D.S. (2018). Concise review: bipotent mega-karyocytic-erythroid progenitors: concepts and controversies. Stem Cell. 36, 1138–1145.

Xi, J., Zhu, H., Liu, D., Nan, X., Zheng, W., Liu, K., Shi, W., Chen, L., Lv, Y., Yan, F., et al. (2013). Infusion of megakaryocytic progenitor products generated from cord blood hematopoietic stem/progenitor cells: results of the phase 1 study. PLoS One 8, e54941.

Xie, X., Fu, Y., and Liu, J. (2017). Chemical reprogramming and transdifferen-tiation. Curr. Opin. Genet. Dev. 46, 104–113.

Xu, J., Du, Y., and Deng, H. (2015). Direct lineage reprogramming: strategies, mechanisms, and applications. Cell Stem Cell 16, 119–134.

Zhang, B., Wu, X., Zi, G., He, L., Wang, S., Chen, L., Fan, Z., Nan, X., Xi, J., Yue, W., et al. (2021). Large-scale generation of megakaryocytes from human em-bryonic stem cells using transgene-free and stepwise defined suspension cul-ture conditions. Cell Prolif. 54, e13002.

Zhang, L., Yin, J.C., Yeh, H., Ma, N.X., Lee, G., Chen, X.A., Wang, Y., Lin, L., Chen, L., Jin, P., et al. (2015). Small molecules efficiently reprogram human as-troglial cells into functional neurons. Cell Stem Cell 17, 735–747.

Zhang, M., Dong, Y., Hu, F., Yang, D., Zhao, Q., Lv, C., Wang, Y., Xia, C., Weng, Q., Liu, X., et al. (2018). Transcription factor Hoxb5 reprograms B cells into functional T lymphocytes. Nat. Immunol. 19, 279–290.

Zhang, M., Lin, Y.H., Sun, Y.J., Zhu, S., Zheng, J., Liu, K., Cao, N., Li, K., Huang, Y., and Ding, S. (2016). Pharmacological reprogramming of fibroblasts into neural stem cells by signaling-directed transcriptional activation. Cell Stem Cell 18, 653–667.

Zhang, Y., Liu, T., Meyer, C.A., Eeckhoute, J., Johnson, D.S., Bernstein, B.E., Nusbaum, C., Myers, R.M., Brown, M., Li, W., and Liu, X.S. (2008). Model-based analysis of ChIP-Seq (MACS). Genome Biol. 9, R137.

Zhao, T., Fu, Y., Zhu, J., Liu, Y., Zhang, Q., Yi, Z., Chen, S., Jiao, Z., Xu, X., Xu, J., et al. (2018). Single-Cell RNA-Seq reveals dynamic early embryonic-like programs during chemical reprogramming. Cell Stem Cell 23, 31–45.e7.

Zhao, Y., Li, X., Zhao, W., Wang, J., Yu, J., Wan, Z., Gao, K., Yi, G., Wang, X., Fan, B., et al. (2019). Single-cell transcriptomic landscape of nucleated cells in umbilical cord blood. GigaScience 8, giz047.

Zhou, Y., Zhu, X., Dai, Y., Xiong, S., Wei, C., Yu, P., Tang, Y., Wu, L., Li, J., Liu, D., et al. (2019). Chemical cocktail induces hematopoietic reprogramming and expands hematopoietic stem/progenitor cells. Adv. Sci. 7, 1901785.

Zhu, S., Li, W., Zhou, H., Wei, W., Ambasudhan, R., Lin, T., Kim, J., Zhang, K., and Ding, S. (2010). Reprogramming of human primary somatic cells by OCT4 and chemical compounds. Cell Stem Cell 7, 651–655.

STAR★METHODS

KEY RESOURCES TABLE

REAGENT or RESOURCE	SOURCE	IDENTIFIER
Antibodies		
PE anti human CD34	eBioscience	Cat#12-0349-42; RRID:AB_1548680
APC anti human CD41a	eBioscience	Cat#17-0419-42; RRID:AB_2573144
BV421 anti human CD41a	Biolegend	Cat#303730; RRID:AB_2629627
PE anti human CD41a	eBioscience	Cat#12-0419-42; RRID:AB_10870785
FITC anti human CD61	eBioscience	Cat#11-0619-42; RRID:AB_10667773
APC anti human CD62p	Invitrogen	Cat#17-0626-82; RRID:AB_11217675
PE anti human CD42b	eBioscience	Cat#12-0429-42; RRID:AB_10852864
FITC anti human CD235a	BD Biosciences	Cat#559943; RRID:AB_397386
BV605 anti human CD71	BD Biosciences	Cat#743306; RRID:AB_2741414
APC anti human CD110	BD Biosciences	Cat#562199; RRID:AB_10894008
PE anti human CD110	BD Biosciences	Cat#562159; RRID:AB_10893807
PE anti human CD123	BD Biosciences	Cat#554529; RRID:AB_395457
BV421 anti human CD123	BD Biosciences	Cat#562517; RRID:AB_11153668
PE anti human CD38	BD Biosciences	Cat#555460; RRID:AB_395853
PE anti human CD53	BD Biosciences	Cat#555508; RRID:AB_395898
Anti-α-Tubulin antibody	Sigma-Aldrich	Cat#T9026; RRID:AB_477593
Anti-von Willibrand Factor	Millipore	Cat#AB7356; RRID:AB_92216
Anti-CD41 antibody	Abcam	Cat#ab134131; RRID:AB_2732852
Human CD61 MicroBeads	Miltenyi Biotec	Cat#130-051-101; RRID:AB_2889174
Human CXCL4/PF4 Affinity Purified Poly-clonal Ab	R&D Systems	Cat#AF795; RRID:AB_355607
Thrombospondin antibody	Abcam	Cat#ab1823; RRID:AB_2201948
CD42b Monoclonal Antibody (HIP1)	eBioscience	Cat#A-21206; RRID:AB_2535792
Alexa Fluor® 568 Donkey Anti-Mouse IgG (H+L)	Invitrogen	Cat#A10037; RRID:AB_2534013
Alexa Fluor® 488 Donkey Anti-Rabbit IgG (H+L)	Invitrogen	Cat#A-21206; RRID:AB_2535792
Alexa Fluor® 647 Donkey Anti-Rabbit IgG (H+L)	Invitrogen	Cat#A-31573; RRID:AB_2536183
Bacterial and virus strains		
PLVX-PF4-promoter-GFP	This paper	N/A
Biological samples		
Human cord blood	This study	N/A
human peripheral blood	This study	N/A
Human bone marrow mononuclear cells	Procell	Cat#CPH238
Chemicals, peptides, and recombinant proteins		
StemSpan SFEM II	STEM CELL Technologies	Cat#09655
Human IL-3	PeproTech	Cat#200-03
Human IL-6	PeproTech	Cat#200-06
Human SCF	PeproTech	Cat#300-07
Human TPO	PeproTech	Cat#300-18
Human EPO	PeproTech	Cat#100-64
L-glutamine	GIBCO	Cat#25030081
Dexamethasone	Sigma-Aldrich	Cat#D1756

(Continued on next page)

Continued

REAGENT or RESOURCE	SOURCE	IDENTIFIER
Human IGF-1	PeproTech	Cat#100-11
CD lipid concentrate	GIBCO	Cat#2337223
Transferrin	Sigma-Aldrich	Cat#T0665
Valproic acid	Selleck	Cat# S3944
RG108	Selleck	Cat# S2821
Bix01294	Selleck	Cat# S8006
PD0325901	Selleck	Cat# S1036
Y27632	Selleck	Cat#S1049
PS48	Selleck	Cat#S7586
CHIR99021	Selleck	Cat# S1263
Forskolin	Selleck	Cat# S2449
2-PCPA	Selleck	Cat#S4246
Ficoll-Hypaque	TBD Science	Cat#LTS1077
Erythrocyte sedimentation fluid	TBD Science	Cat#HES-TBD550
Calcein-AM	Sigma-Aldrich	Cat#17783
Human Fibrinogen	Sigma-Aldrich	Cat#F3879
Hoechst 33342	BD Biosciences	Cat#561908
Percoll	Solarbio	Cat#P8370
PGE1	Selleck	Cat#S1508
Apyrase	Sigma-Aldrich	Cat#A6535
Carboplatin	Selleck	Cat# S1215
TRAP6	Sigma-Aldrich	Cat#T1573
ADP	Sigma-Aldrich	Cat# 01905
Clodronate liposomes	Liposoma B.V.	Cat#C-005
Colchicin	Sigma-Aldrich	Cat# C3915
Thrombin	Sigma-Aldrich	Cat#T7009
4% Fixative solution	Solarbio	Cat#P110
Dead Cell Removal Kit	Miltenyi Biotec	Cat#130-090-101
RNeasy Mini Kit	Qiagen	Cat#74104
SYBR qPCR Mix	TOYOBO	Cat#QPS-201
ReverTra Ace qPCR RT Master Mix	TOYOBO	Cat#FAQ-201
Critical commercial assays		
Human PF4 ELISA Kit	BOSTER	Cat#EK0726
Human THBS1 ELISA Kit	Solarbio	Cat#SEKH-0322
Deposited data		
Raw and analyzed sequencing data	This paper	GSE207654
Experimental models: Organisms/strains		
NOD-Prkdc^{scid} IL2rg^{tm1}/Bcgen	Biocytogen	N/A
Oligonucleotides		
See Table S1	N/A	N/A
Software and algorithms		
FlowJo	FlowJo	https://www.flowjo.com
GraphPad Prism 7	GraphPad	https://www.graphpad.com/
NIS Elements	Nikon	https://www.microscope.healthcare.nikon.com/
AMT Capture Engine Software Version 600.259	AMT	https://amtimaging.com/
Volocity	PerkinElmer	https://www.perkinelmer.com

(Continued on next page)

Continued

REAGENT or RESOURCE	SOURCE	IDENTIFIER
Zen	Carl Zeiss	https://www.zeiss.com
iQ5	Bio-Rad	https://www.bio-rad.com
SoftMax Pro	Molecular Devices	https://www.moleculardevices.com
CellRanger v3.0.2	10X Genomics	https://github.com/10XGenomics/cellranger
Monocle3	Cao et al., 2019	https://cole-trapnell-lab.github.io/monocle3/
Seurat v3	Stuart et al., 2019	https://satijalab.org/seurat/
R v4.1.0	R-Project	https://www.r-project.org/
DAVID	Huang da et al., 2009	https://david.ncifcrf.gov/
MACS2	Zhang et al., 2008	http://github.com/taoliu/MACS/
HOMER	Heinz et al., 2010	http://homer.ucsd.edu/homer/motif/
BedTools	Bedtools	https://bedtools.readthedocs.io
DeepTools	Ramírez et al., 2016	https://deeptools.readthedocs.io

RESOURCE AVAILABILITY

Lead contact
Further information and request for resources and reagents should be directed to and will be fulfilled by the Lead Contact, Yanhua Li (shirlylyh@126.com).

Materials availability
All unique/stable reagents generated in this study are available from the lead contact with a completed Materials Transfer Agreement.

Data and code availability
The scRNA-seq and ATAC-seq data has been uploaded to GEO: GSE207654. This paper does not report original code. Any additional information required to reanalyze the data reported in this work paper is available from the lead contact upon request.

EXPERIMENTAL MODEL AND SUBJECT DETAILS

Animals
B-NDG (NOD-Prkdc^{scid} IL2rg^{tm1}/Bcgen) mice were purchased from Biocytogen Pharmaceuticals Co., Ltd (Beijing, China). All mice were kept under specific pathogen-free conditions, and all procedures were performed according to protocols approved by the Institutional Animal Care and Use Committee in compliance with Beijing Medical Experimental Animal Care Commission.

Human subjects
Human cord blood samples were obtained from Beijing Cord Blood Bank. Women with healthy, full-term pregnancies who met the Beijing Cord Blood Bank criteria for inclusion and gave informed consent were eligible to donate cord blood. Human bone marrow-derived mononuclear cells were obtained from Procell life Science & Technology Co., Ltd (Wuhan, China) from consented healthy donors. Human peripheral blood samples were obtained from Department of Transfusion, the Fifth Medical Center of Chinese PLA General Hospital. All procedures involving human subjects in this study were approved by Ethics Committee of the AMMS (Approval No.: AF/SC-08/02.178).

METHOD DETAILS

Purification of human CB-derived erythroblasts
Human CB mononuclear cells (MNCs) were separated by Ficoll-Hypaque density gradient centrifugation (1.077 g/L; TBD Science, Tianjin, China). MNCs were cultured at 3×10^6 cells/mL in StemSpan SFEM II medium (StemCell Technologies, Vancouver, Canada) supplemented with 100 ng/mL stem cell factor (SCF, Peprotech, Rocky Hill, NJ, USA), 40 ng/mL insulin-like growth factor-1 (Peprotech), 5 U/mL human recombinant erythropoietin (Peprotech), 100 μg/mL holo-transferrin (Sigma-Aldrich, St. Louis, MO, USA), 1 μM dexamethasone (Sigma-Aldrich), 2 mM L-glutamine (Gibco, Grand Island, NY, USA), and 1:500 CD lipid concentrate (Gibco). After 7 days of culture, the cells were harvested, stained, and sorted using anti-CD34-PE, anti-CD41a-PE, anti-CD42b-PE, anti-CD110-PE, anti-CD123-APC, and anti-CD235a-FITC antibodies to obtain CD34$^-$CD123$^-$CD41a$^-$CD42b$^-$CD110$^-$CD235a$^+$ cells.

Conversion of erythroblasts to iMKs

CD34$^-$CD123$^-$CD41a$^-$CD42b$^-$CD110$^-$CD235a$^+$ cells were cultured in iMK induction medium containing StemSpan SFEM II medium supplemented with 0.5 μM Bix01294 (Selleck, Houston, TX, USA), 0.04 μM RG108 (Selleck), 0.5 μM PD0325901 (Selleck), 0.2 mM valproic acid (VPA, Selleck), 50 ng/mL SCF, 50 ng/mL thrombopoietin (TPO, Peprotech), 20 ng/mL IL-3 (Peprotech), and 50 ng/mL IL-6 (Peprotech). After 7 days, the cells were transferred to StemSpan SFEM II medium supplemented with 20 ng/mL SCF, 50 ng/mL TPO, 20 ng/mL IL-3, and 50 ng/mL IL-6 for specification. The medium was refreshed every 2–3 days.

Proplatelet formation and platelet production

iMKs were cultivated on human fibrinogen (50 μg/mL; Sigma-Aldrich)-coated plates in StemSpan SFEM II medium supplemented with 20 ng/mL SCF and 50 ng/mL TPO, the plates were placed on a Digital Mini Rotator (Thermo Scientific) at 95 rpm.

PF4 reporter lentivirus transduction

The human PF4 promoter-GFP reporter vector PLVX-PF4-promoter-GFP was constructed as previously described (Jiang et al., 2022). CD34$^-$CD123$^-$CD41a$^-$CD42b$^-$CD110$^-$CD235a$^+$ cells were transduced with PLVX-PF4-promoter-GFP lentivirus and cultured in iMK induction medium. GFP-positive cells were monitored on days 1, 5, and 7 using confocal microscopy and flow cytometry.

Flow cytometry

Single-cell suspensions were stained with cell-surface antigens in PBS at 4°C for 40 min. The stained cells were analyzed or sorted using a BD FACSAria (BD Biosciences, Franklin Lakes, NJ, USA) and the data were analyzed using FlowJo software (TreeStar, Ashland, OR, USA).

Morphologic analysis

Cells were rinsed in PBS, cytocentrifuged onto glass slides, stained with Wright–Giemsa solution (Baso), and then observed by light microscopy (Nikon, Tokyo, Japan). NIS-Elements F software (Nikon) was used to capture the images.

Immunofluorescence staining

Cultured cells were cytocentrifuged onto glass slides, fixed with 4% paraformaldehyde for 20 min at room temperature, rinsed with PBS, blocked with 10% donkey serum in PBS for 1 h, and incubated with primary antibodies at 4°C overnight. Labeled isotype-specific secondary antibodies were added when necessary and incubated for 1 h at room temperature. The cells were counterstained with 4′,6-diamidino-2-phenylindole for visualization of cell nuclei and observed using a Zeiss LSM 880 confocal microscope (Zeiss, Oberkochen, Germany) and Zeiss ZEN microscope software (Zeiss).

Quantitative real-time PCR analyses

Total RNA was isolated using an RNeasy extraction kit (Qiagen, Hilden, Germany). RNA was reverse-transcribed using high efficient reverse transcriptase ReverTra Ace (TOYOBO, Osaka, Japan) according to the manufacturer's instructions. qPCR was performed using SYBR Green real-time PCR master mix (TOYOBO) on a Bio-Rad iQ5 Real-Time PCR detection system (Hercules, CA, USA). Data were analyzed using the ΔΔCt method. The primers are listed in Table S1.

Measurement of THBS1 and PF4

We quantified THBS1 and PF4 levels in the culture suspensions and cell lysates of 1×10^6 cells from each group using ELISA. The human THBS1 ELISA Kit (Solarbio, Beijing, China) and PF4 ELISA Kit (BOSTER, Wuhan, China) were used according to the manufacturer's protocol.

Transmission electron microscopy

The cells or platelets were rinsed with PBS and fixed in 3% glutaraldehyde/0.1 M sodium cacodylate, pH 7.4. Following three rinses with sodium cacodylate buffer, the samples were postfixed for 1 h in 1% osmium tetroxide/0.1 sodium cacodylate buffer. After rinsing in deionized water, the samples were dehydrated and embedded in Polybed 812 epoxy resin (Polysciences, Inc., Warrington, PA, USA). The samples were sectioned perpendicularly to the substrate at a thickness of 70 nm using a diamond knife. Ultrathin sections were collected on 200 mesh copper grids and stained with 4% aqueous uranyl acetate for 15 min, followed by staining with Reynolds' lead citrate for 7 min. The samples and stained sections were observed using an H7650 transmission electron microscope (Hitachi, Tokyo, Japan) operating at 80 kV and photographed using an AMT XR16M CCD digital camera and AMT Capture Engine Software Version 600.259 (AMT, Woburn, MA, USA).

Ploidy analysis

Cells were immunostained for determining CD41a and CD42b expression and then incubated with 10 μg/mL Hoechst 33342 (BD Biosciences) for 30 min before flow cytometry.

MK isolation from human BM
Human MKs were purified from the BM by using a modified method of Percoll density gradients and magnetic-activated cell sorting. Briefly, human BM cells were placed on two layers of percoll solution with different densities (1.02 g/mL and 1.05 g/mL), and the MKs were in the fraction greater than 1.02 g/mL and less than 1.05 g/mL. After centrifugation at 400×g for 20 min, the cells in the middle layer were collected and stained with anti-human CD61 magnetic microbeads at 4°C for 30 min in the dark. The CD61$^+$ MKs were sorted using magnetic-activated cell sorting.

Preparation of human PB-PLTs and iMK-PLTs
Human platelet-rich plasma was prepared by centrifugation of sodium citrate-treated human peripheral blood at 120 × g for 20 min. The supernatant was collected and centrifuged at 400 × g for 20 min in the presence of 1 μM PGE1 (Selleck) and 1 U/mL Apyrase (Sigma-Aldrich). The pellet was washed and resuspended in HEPES-Tyrode's buffer containing 1 μM PGE1 and 1 U/mL Apyrase. For iMK-PLTs, the culture media containing iMK-PLTs were gently collected with 1 μM PGE1 and 1 U/mL Apyrase to prevent platelet activation. The iMK-PLTs were enriched and washed, as described above.

Flow cytometric analysis of platelet activation
Fresh human PB-PLTs and iMK-PLTs were stained with CD41a-BV421, CD42b-PE and CD62P-APC antibodies, stimulated with 2 U/mL thrombin (Sigma-Aldrich), 100 μM TRAP6 (Sigma-Aldrich) and 20 μM ADP (Sigma-Aldrich) for 15 min at 37°C with shaking at 1000 rpm, fixed in 1% paraformaldehyde and analyzed by flow cytometry.

Spreading assay
Blood platelets and iMK-derived platelets suspended in Tyrode-HEPES buffer with 2 U/mL thrombin were seeded into fibronectin-coated glass-bottom culture dishes and incubated for 45 min at 37°C. The cells were fixed using 4% formaldehyde, immunostained with α-tubulin and CD41, and observed under a Zeiss LSM 880 confocal microscope.

Clot formation and retraction
Human blood PLTs or iMK-PLTs (approximately 1.5×10^7/mL) were resuspended in 200 μL platelet-depleted plasma in siliconized glass tubes. Thrombin (2 U/mL) was added to induce clot formation and retraction. The clots were allowed to retract at 37°C for 1 h and then photographed.

In vivo MK infusion experiments
On day −3, carboplatin (Selleck) was reconstituted with sterile 0.9% NaCl and injected intraperitoneally into 8–12-week-old male B-NDG mice (NOD-Prkdc^{scid} IL2rg^{tm1}/Bcgen, Biocytogen, Beijing, China) at a dose of 125 mg/kg to induce thrombocytopenia (Ulich et al., 1995). On day −1, the mice were depleted of macrophages by treatment with 0.04 mg clodronate liposomes (Liposoma Technology, Amsterdam, Netherlands) per gram of mouse weight. EBs or iMKs were stained with 2 μg/mL calcein-AM (Sigma-Aldrich) for 30 min at 37°C before washing. PBS (400 μL) containing 1×10^7 cells was injected into mice through the tail vein. Human platelets were monitored by flow cytometry from peripheral blood samples at days 1 and 3 after transfusion using antibodies specific for human CD41a. The absolute platelet count was determined using a Celltac E MEK7222 hematology analyzer (Nihon Kohden, Tokyo, Japan). The mice were sacrificed on day 3, and samples from bone marrow were collected. All mice were kept under specific pathogen-free conditions, and all procedures were performed according to protocols approved by the Institutional Animal Care and Use Committee.

Analysis of platelet adhesion and aggregation under controlled flow
Experiments under flow were performed using a BioFlux 1000z system (Fluxion, San Francisco, CA, USA) (Fuentes et al., 2013). The microfluidic chambers were coated with 100 μL collagen (40 μg/mL) for 1 h. Thereafter, the channels were perfused with PBS containing 0.5% bovine serum albumin for 15 min. Blood samples were collected by heart puncture from anesthetized mice, anticoagulated with sodium citrate, and centrifuged at 180 × g for 10 min to obtain PRP. PRP was treated with or without epifibatide and immunostained with anti-human CD41a-PE (eBioscience, San Diego, CA, USA) before being added to the inlet wells. The chambers were perfused for 5 min at room temperature (at 20 dyne/cm^2). Platelet deposition was observed and recorded using a Zeiss Z1 inverted fluorescence microscope.

Karyotype analysis
EBs and iMKs were incubated with 10 μg/mL colchicin (Sigma-Aldrich) for 3 h to accumulate cells in metaphase. After hypotonic treatment and fixation of the cells, metaphase chromosome spreads were prepared according to standard protocols (Stallard, 1998). The clearly spread chromosomes were counted in at least 20 individual cells.

scRNA-seq
Freshly sorted EBs (day 0) and viable cells from the iMK induction culture on days 3, 5, and 7 were collected and analyzed using the Chromium system (10x Genomics) according to the manufacturer's instructions for an expected capture rate of approximately 8,000 single cells per sample (performed by Annoroad Gene Technology, Beijing, China).

Primary process and quality control of scRNA-seq data

Raw sequencing data were converted to fastq files using Illumina bcl2fastq (version 2.20; San Diego, CA, USA) and aligned to the human genome reference (*Homo sapiens* UCSC.hg19 x). The CellRanger analysis pipeline was used to generate a digital gene expression matrix from these data. The raw digital gene expression matrix data were further filtered as follows: cells with a very small library size (<2,500) and a very high (>0.15) mitochondrial genome transcript ratio were removed. After filtering, the data were processed using the standard workflow implemented in Monocle3.

Visualization and clustering

After normalization, the batch effects were removed using the mutual nearest neighbor alignment method (Haghverdi et al., 2018). We then applied principal component analysis on the most variable genes (k = 2,000) across all cells to reduce the number of dimensions representing each cell. To visualize the cells in a two-dimensional space, the first 50 components were applied for t-SNE analysis according to the elbow of the scree plot. To group the cells into clusters, a community detection method, Leiden clustering algorithm, with a resolution parameter of 1.5e-5 was applied to the preprocessed data. Differential expression between clusters was calculated using a likelihood-ratio test for single-cell gene expression at a family wise error rate of 5%.

Trajectory analysis

To further investigate the dynamic changes during chemical reprogramming, the single-cell trajectory analysis module in Monocle3 was used to reconstruct pseudotime trajectories according to the documentation (https://github.com/cole-trapnell-lab/monocle-release). The uniform manifold approximation and projection method was used to apply dimensionality reduction, which was visualized using the plot_cell function. Cells were fit into a principal trajectory graph using the learn_graph function, and the trajectory "root" of the trajectory was manualy picked as the "beginning" of the predicted biological process. To learn the overall gene expression changes along the pseudotime, a graph_test function with parameter neighbor_graph = "principal_graph" was used to test whether cells at similar positions on the trajectory have correlated expression for the gene being tested. Genes with a q value less than 0.05 were considered as statistically significant. The expression of genes was smoothed and visualized using the plot_genes_in_pseudotime function.

Cell cycle regression

The difference in cell cycle stages between cells can contribute to heterogeneity in the scRNA-seq datasets. The CellCycleScoring function implemented in Seurat was used to evaluate the cell cycle status based on the expression of previously reported G1/S and G2M phase-specific genes (Macosko et al., 2015; Tirosh et al., 2016). The cell cycle scores were then regressed using a linear model.

GO enrichment analysis

GO and pathway enrichment (using the Kyoto Encyclopedia of Genes and Genomes database) analyses were performed using DAVID (version 6.8, https://david.ncifcrf.gov).

Cell type correlation analysis

A total of 14,298 scRNA-seq datasets from fresh cord blood and peripheral blood samples, corresponding to five major hematopoietic lineage cell types, were obtained from a previous study (Zhao et al., 2019). In order to measure the similarity between iMKs and different natural hematopoietic cell types, we calculated Spearman's rank correlation between the average gene expression of each cell cluster. The correlation matrix was visualized using Corrplot R package (v0.92) [Wei T, Simko V (2021). R package 'corrplot': Visualization of a Correlation Matrix. https://github.com/taiyun/corrplot.].

TF network construction

To construct a TF correlation network during the conversion of EBs to MKs, the normalized gene expression of the statistically significant TFs was used to calculate Spearman's rank correlation coefficients, which were then applied to generate the correlation matrix. A network plot was constructed using the ggraph R package (v2.0.5).

ATAC-seq

Two biological replicates for each of the D0, D3, D5, and D7 cells, prepared in the same way as RNA-seq, were processed for construction of ATAC-seq libraries using the methods previously described (Buenrostro et al., 2015; Corces et al., 2017). In brief, cells were dissociated from each pooled sample to obtain single-cell suspensions. Then, cells were suspended in nuclear isolation buffer and washed repeatedly using nuclear wash buffer following a standard nuclear isolation protocol. A total of 40,000 nuclei were pelleted and re-suspended with transposase for 30 min at 37°C. The transposed DNA was purified with a MinElute Kit (Qiagen) and was used to generate the library via PCR amplification. All libraries were purified using a Qiagen MinElute PCR Purification Kit following the manufacturer's instruction and were sequenced on an Illumina Novaseq 6000 platform.

ATAC-seq bioinformatics analysis

After removal of the adaptor sequences, the reads were aligned to the hg38 human reference genome using the BWA-MEM software. The model-based analysis of ChIPseq (MACS2 v2.1.2) was applied to call the ATAC-seq peak regions of each sample by using a bam

file of uniquely mapped reads as the input, and the q-value cutoff for peak calling was 0.05. Peak annotation was performed by HOMER v4.9.1 function annotatePeaks.pl, which picks putative target genes that are located within ATAC-seq called peaks or contain the transcription start sites (TSSs) nearest to these peaks. Motif analysis on peak regions was performed by HOMER v4.9.1 function findMotifsGenome.pl. Distribution of uniquely mapped reads resulting from ATAC-seq in a bigwig file across either peaks or gene body was analyzed using deeptools v3.2.1. To identify differential peaks between different stages of development, the ATAC-seq peaks of each sample were merged to generate a consensus set of unique peaks, among which the number of peaks was further counted for each sample using bedtools v2.25.0, and differential peaks were identified by DESeq2 (v1.16.0), with the thresholds of | log2FC| > 1 and p < 0.05. ATAC-seq and data analysis were performed by Shanghai Jiayin Biotechnology Co., Ltd.

QUANTIFICATION AND STATISTICAL ANALYSIS

All statistical data are expressed as the mean ± standard error of the mean (SEM). The sample size used is indicated in the figure legends. Statistical analyses were performed using GraphPad Prism version 7 software (GraphPad, Inc., La Jolla, CA, USA). For most statistical evaluation, a two-tailed Student's *t* test was applied to calculate the statistical probability. Statistical significance was set at p < 0.05.